



Distinguishing interannual variations and possible impacted factors for the northern and southern mode of South Asia High

Xu Xue¹ · Wen Chen²

Received: 20 January 2019 / Accepted: 27 May 2019 / Published online: 31 May 2019
© Springer-Verlag GmbH Germany, part of Springer Nature 2019

Abstract

Given the large meridional coverage of South Asian High (SAH), the interannual variabilities of SAH and the corresponding impacted factors may differ between mid- to high-latitude and low-latitude components of SAH. This study distinguishes the interannual variations of the mid- to high-latitude and low-latitude components of SAH to obtain further understanding of SAH variations. By means of composite analysis, this study investigates the characteristics of the northern and southern mode of SAH variation (N-SAH, S-SAH). When the SAH is regarded as an entirety (E-SAH) based on numerous previous studies, it strengthens distinctly and expands toward both meridional and zonal directions in strong E-SAH comparing to weak E-SAH. The geopotential height (HGT) and tropospheric temperature (TT) anomalies related to the E-SAH are concurrently observed over the low-latitude and mid- to high-latitude regions. In contrast, when N-SAH and S-SAH are defined in this study, the SAH is distinctly strengthened only over its northern (southern) side and expands northward (southward) in strong N-SAH (S-SAH) comparing to the weak group. The HGT and TT anomalies related to the N-SAH (S-SAH) cases are limited over the mid- to high-latitude (low-latitude) regions. Possible impacted factors related to E-SAH, N-SAH, and S-SAH are further analyzed. The N-SAH is closely associated with precipitation anomalies over Indian Peninsula, meridional circulation over Tibet Plateau (TP), land surface temperature (LST) anomalies over Indian Peninsula and northern TP, meridional LST gradient between Indian Peninsula and northern TP, and circumglobal teleconnection (CGT). For instance, positive rainfall anomalies together with obviously ascending motion over Indian Peninsula contributes to a decreased LST anomalies via cloud-radiation feedback here, which forms a north-to-south LST gradient. The LST gradient will reduce the climatological south-to-north LST gradient here, which in turn contributes to a northward meridional circulation over northern TP, and finally contribute to a strong N-SAH existing over north of 25°N. Furthermore, the positive rainfall anomalies over Indian Peninsula tends to inspire a strong CGT over mid-high latitude through atmospheric response to condensation latent heating source, which in turn contributes to a strong N-SAH. In contrast, the meridional circulation associated with S-SAH is exhibited by southward shifting over southern TP (south of 30°N) due to atmospheric response to heating source generated by significant SST anomalies over Indian Ocean. Obviously warm center is observed in low-upper troposphere from tropical region to southern TP, which finally result in a strong S-SAH, accompanied by shifting southward. However, variation of E-SAH is a result of the combined action of rainfall anomalies over Indian Peninsula and SST anomalies over Indian Ocean. These differences indicate that it is necessary and of scientific significance to distinguish the northern and southern mode of the SAH.

Keywords South Asian High · Northern and southern mode · LST · Rainfall · Meridional circulation · CGT · ENSO

1 Introduction

South Asia High (SAH; also referred to as Asian monsoon anticyclone or Tibetan high) is a large semi-permanent anticyclonic system steadily situated in the upper troposphere and lower stratosphere during the boreal summer, covering the entire eastern hemisphere from North Africa to the Date Line in subtropics (Fig. 1a; Mason and Anderson 1963;

✉ Xu Xue
xuexu.zs@163.com

¹ Department of Ecology, College of Life Science, Guizhou University, Guiyang 550025, Guizhou, China

² Center for Monsoon System Research, Institute of Atmospheric Physics, Chinese Academy of Sciences, Beijing, China

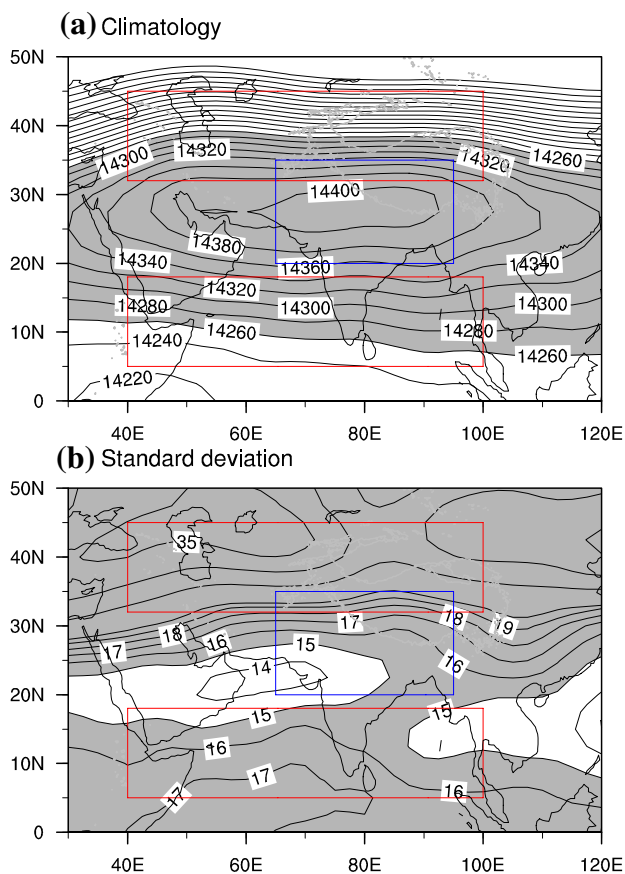


Fig. 1 **a** Climatological mean and **b** standard deviation of June–July–August (JJA) mean geopotential height (HGT) at 150-hPa during 1980–2017. The contour interval is 20 gpm in **a** and uneven in **b**. Shading is applied for stressing purpose. The two red and blue boxes denote the regions (32° – 45° N, 40° – 100° E), (5° – 18° N, 40° – 100° E) and (20° – 35° N, 65° – 95° E) used to define the N-SAH, S-SAH and E-SAH index, respectively

Tao and Zhu 1964; Tao and Chen 1987; Krishnamurti 1971; Zhang et al. 2002). As a prominent high-pressure system, the SAH could employ substantial impacts on variability of weather, climate, and chemical composition over Asian and remote areas (Zhang et al. 2005; Zhao et al. 2009; Chen et al. 2009; Wei et al. 2014, 2015; Shi and Qian 2016; Cai et al. 2017; Ning et al. 2017; Ge et al. 2018; Park et al. 2004; Randel and Park 2006). For instance, the climate associated with SAH can exert profound influences on tropical cyclone activity over the western North Pacific through modulating the tropical upper tropospheric trough (TUTT) (Sadler 1976), which is owing to that the strong westerly wind shear related to TUTT usually restricts the eastward propagation of the tropical cyclone over the west North Pacific (Kelley and Mock 1982; Fitzpatrick et al. 1995; Wu and Wang 2015). The relationship between Meiyu and the SAH is investigated by Li et al. (2018) to reveal that years with stronger SAH in April are generally concurrent with earlier onset of

Meiyu and increased precipitation in June over the Yangtze-Huai River basin. Ning et al. (2017) pointed out that the northwest-southeast movement and strength of SAH have a profound impact on the summer extreme precipitation over eastern China, with more (less) extreme rainfall over Jiang-Huai River Basin when the SAH shifts anomalously north-westward. As the strongest and steadiest system in the upper troposphere, the SAH could also have a profound implication on the distribution and variability of trace constituents and aerosol in the upper troposphere and lower stratosphere (Dethof et al. 1999; Park et al. 2004, 2008; Li et al. 2005; Randel and Park 2006). Hence, a further investigation of SAH variability is of great significance to well improving weather and climate prediction.

On account of the large socioeconomic influences of the Asian summer monsoon, the variability of SAH and related climate effects have long been a fascinating scientific hot-spot. Existing researches mainly pay heeds to two topics: intensity of the SAH and position of the SAH center. For the former topic, the intensity of SAH shows large inter-annual and interdecadal variations and is closely linked to summer extreme climate events and rainfall over Asia and remote areas (Zhang et al. 2000, 2005; Qian et al. 2002; Xue et al. 2014, 2015, 2017, 2018; Zhao et al. 2009). For the latter one, more attentions are exerted on the variations of the SAH center in zonal direction (Mason and Anderson 1963; Tao and Zhu 1964; Luo et al. 1982; Qian et al. 2002; Wei et al. 2014; Ren et al. 2015; Shi and Qian 2016). For instance, Mason and Anderson (1963) firstly pointed out that the longitudinal movement of the SAH and has been regarded as the most crucial characteristic of the SAH activities ever since then. Luo et al. (1982) classified the SAH as the west pattern, the east pattern, and the transitional pattern based on its center location. Through counting the location of the SAH center for numerous years, Qian et al. (2002) defined the two balance patterns of the SAH, including the Tibetan high located over the east of 75° E and Iranian high situated in the west of 75° E. Tao and Zhu (1964) indicated that the east–west shift of the SAH exists a quasi-biweekly time scale. Wei et al. (2014) pointed out that in the inter-annual timescale the east–west shift is a prominent feature of the SAH via defining the east–west shift index of the SAH. Their results indicated that the east–west position of SAH has close connection to the summer rainfall over China, for instance, a westward (eastward) shifting of SAH generally occurs together with less (more) rainfall in the Yangtze-Huai River Valley and more (less) rainfall in North China and South China. By using the daily atmospheric data, Shi and Qian (2016) also investigated the connection between anomalous zonal activities of the SAH and Eurasian climate.

Meanwhile, several existing researches focus on movement of the SAH center in meridional direction. For instance, the north–south seasonal shift of the SAH ridge is

closely related to the location of the rain belt in China, with earlier and stronger Meiyu appearing over Jiang-Huai River Basin when the SAH jumps to 25°–30°N ahead of time (Zhu et al. 1980). Wei et al. (2012) constructed the north–south shifting index of the SAH as the standardized difference between geopotential heights averaged over (27.5°–32.5°N, 50°–100°E) and (22.5°–27.5°N, 50°–100°E). The index can well depict the north–south shift of the SAH and is closely connected with summer rainfall over China. Further, the north–south shifting of the SAH is prominently influenced by preceding winter El Niño–Southern Oscillation (ENSO) (Zhang et al. 2000; Xue et al. 2015, 2018). However, through further analyzing their results, we find that the impacts of ENSO events on SAH are mainly limited to south side of SAH. Variabilities of SAH and corresponding influenced factors may differ between the mid- to high-latitude and low-latitude components of SAH. Furthermore, it is well known that one feature unique to the SAH is which has a large meridional coverage, extending from the tropical Indian Ocean all the way to the north of Tibetan Plateau (from 10°N to 45°N, Fig. 1a). Numerous previous studies only regarded SAH as an entirety to investigate its variability and climate impacts (Zhang et al. 2000, 2005; Xue et al. 2014, 2015, 2017, 2018). For instance, the intensity index of the SAH in Zhang et al. (2005) is defined as the area-averaged geopotential height over the region of (20°–35°N, 65°–95°E), where the climatological SAH center is usually located. It is considerably appropriate to depict the variations and climate impacts of the SAH according to their results. However, it is still unclear whether the above-mentioned intensity index can reasonably indicate the variations of the northern or southern side of the large-scale SAH. Simultaneously, whether similar variation features and influenced factors are concurrently revealed for the large-scale SAH in the mid- to high-latitude and low-latitude regions are still unclear even until now. Therefore, it is of great significance to further investigate the variations and influenced factors associated with the large-scale SAH in the mid- to high and low-latitude regions by exploring new indices. We will present evidence to reveal that new different variation characteristics and impacted factors are observed for the northern and southern mode of SAH comparing to those results which only regarded SAH as an entirety.

The organization of this paper is as follow. A brief description of datasets and methods is given in Sect. 2. Definitions of the northern and southern mode of the SAH are discussed in Sect. 3. Section 4 introduces the associated variations of the northern and southern mode of the SAH. Possible impacted factors related to the two modes are described in Sect. 5, which has four subsections. Section 5.1 describes rainfall anomalies and meridional circulation associated with E-SAH, N-SAH, and S-SAH. The relationship of land surface temperature (LST) with E-SAH, N-SAH, and

S-SAH is presented in Sect. 5.2. Furthermore, the circum-global teleconnection (CGT) and the tropical SST related to ENSO event are introduced in Sects. 5.3 and 5.4, respectively. A summary is shown in Sect. 6.

2 Data and methods

The atmospheric products applied in the present study, including monthly mean geopotential height (HGT), zonal and meridional winds, and air temperature, were derived from the National Centers for Environmental Prediction/National Center for Atmospheric Research (NCEP/NCAR) reanalysis from 1948 to the present (Kalnay et al. 1996). It has a horizontal resolution of 2.5°×2.5° in longitude and latitude with 17 standard pressure levels vertically. Meanwhile, the corresponding variables obtained from the European Centre for Medium-Range Weather Forecasts (ECMWF) interim reanalysis (ERA-Interim) product (Dee et al. 2011) were also used to insure the authenticity of results. The land surface temperature (LST) and precipitation data was extracted from the Climatic Research Unit (CRU) Time-Series (TS) version 4.01 (CRU TS4.01) of high horizontal resolution with 0.5°×0.5°, which encompasses the period of 1901–2016 (Harris and Jones 2017; http://data.ceda.ac.uk/badc/cru/data/cru_ts/cru_ts_4.01/data/tmp/). Monthly mean sea surface temperature (SST) data was obtained from the Hadley Centre global sea ice and sea surface temperature (HadISST) with a horizontal resolution of 1°×1° covering the period from 1870 to the present day (Rayner et al. 2006).

Niño3 index defined by the area-averaged SST over the region (5°S–5°N, 150°W–90°W) was applied to describe the El Niño–Southern Oscillation (ENSO) signal. The circumglobal teleconnection index was defined by using the interannual variability of the 150-hPa HGT averaged over the west-central Asia region (35°–40°N, 60°–70°E) based on Ding and Wang (2005). Eight types of SAH intensity indices are employed, termed as *Iarea*, *Iinta*, *Iintb*, *Iintc*, E-SAH1, *I_{sn}*, *I_n*, and *I_s*, respectively, which are shown in Table 1. The area index of the SAH (*Iarea*) is calculated as the number of grid cells where HGT at 150-hPa exceeds 14,360 geopotential meters (gpm) over the region (0°–45°N, 0°–180°E) based on Zhang et al. (2000). The maximum HGT at 150-hPa over the region (0°–45°N, 0°–180°E) is defined as *Iinta*. *Iintb* is calculated as summation of the difference between HGT in all grids over the region (0°–45°N, 0°–180°E) and 14,360 gpm at 150 hPa level. The ratio between *Iintb* and *Iarea* is termed as *Iintc* (Zhang et al. 2000). E-SAH1 is defined as the area-averaged HGT at 150-hPa over the region of (20°–35°N, 65°–95°E) to depict the variations of the SAH regarded as an entirety (referred to as E-SAH in the following study, Zhang et al. 2005). The difference of 150-hPa HGT averaged over the region of (27.5°–32.5°N,

Table 1 Descriptions of the existing SAH indices

Name	Definition	Reference
<i>I</i> area	Number of grid cells where HGT of 150-hPa exceeds 14,360 gpm in the region (0°–45°N, 0°–180°E)	Zhang et al. (2000)
<i>I</i> inta	Maximum HGT over the region (0°–45°N, 0°–180°E) at 150 hPa	Zhang et al. (2000)
<i>I</i> intb	Summation of the difference between HGT in all grids over <i>I</i> area and 14,360 gpm at 150 hPa	Zhang et al. (2000)
<i>I</i> intc	<i>I</i> intb/ <i>I</i> area	Zhang et al. (2000)
E-SAHI	The regional average over (20°–35°N, 65°–95°E) at 150 hPa	Zhang et al. (2005)
<i>I</i> sn	Difference between HGT averaged over (<i>I</i> n 27.5°–32.5°N, 50°–150°E) and those averaged over (<i>I</i> s 22.5°–27.5°N, 50°–105°E) at 150 hPa	Wei et al. (2012)

50°–100°E, *I*n) and (22.5°–27.5°N, 50°–100°E, *I*s) is termed as *I*sn (Wei et al. 2012).

In the present study, the main analyzed period is focusing on the period of 1980–2017. Anomalies of variable are obtained by calculated with respect to the analyzed period, except for the LST with respect to the period of 1980–2016. The component of interannual variation was gained by removing the interdecadal variation from the original variables based on a 9-year running mean filtering analysis.

The EOF and rotated EOF (REOF) are employed in the present study to extract the dominant spatial pattern of the summer 150-hPa HGT anomalies. Composite analysis method is mainly employed to obtain distribution of anomalies. The Student's *t* test is employed to examine the significance of the composite anomalies and the correlation coefficient (CC).

3 Definition of the northern and southern mode of the South Asia high

To further distinguish the interannual variations of SAH over the mid- to high-latitude and low-latitude region, the northern and southern mode of the SAH need to be urgently defined. Figure 1 displays the summer (June–July–August mean, JJA) mean HGT at 150 hPa and the corresponding standard deviation. The climatological SAH features a zonally elongated ellipse circled by the 14,260 gpm contour stretching from 10° to 40°N and 10° to 140°E, with its main center over the southwestern side of the Tibetan Plateau (TP) (Fig. 1a). Two regions with relatively large standard deviation are observed in Fig. 1b. One is situated over the mid- to high-latitude land region, for instance, the Caspian Sea and northeastern China from 30° to 50°N. The other one is located over the Indian Ocean, expanding from 18°N to south of the equator (Fig. 1b).

Preceding researches revealed that the summer HGT at 150-hPa level over Asia can well reflect the strength of SAH (Zhang et al. 2000; Wei et al. 2014; Xue et al. 2014). To reveal the spatial pattern of the SAH, an EOF analysis for summer with 150-hPa HGT anomalies during 1980–2017

was performed over the region of (0°–50°N, 30°–120°E) where the SAH is usually situated (Fig. 2a, b). The first EOF mode accounts for approximately 38.8% of the total variance and indicates a pattern of consistent strengthening (weakening) of the summer HGT over the entire region of (0°–50°N, 30°–120°E). In the second EOF mode, which also explains a large variance with nearly 29.3%, two large and opposite loading centers are observed over the Caspian Sea/northeastern China (27.5°–50°N) and the region of southern TP expanding to Indian Ocean (0°–27.5°N) (Fig. 2b). Based on the distribution of the standard deviation and the loading of the first two EOF modes, the result indicates that inconsistent and even opposite variabilities of the SAH at different meridional latitudes can usually be observed. It is noted that the above two large and opposite loading regions in the second EOF mode over the mid- to high-latitude and low-latitude regions are nearly in accordance with the two regions in the standard deviation (Fig. 1b). According to the climatological location of the SAH, the results of standard deviation and EOF (Figs. 1 and 2a, b), the area-averaged summer 150-hPa HGT over the mid- to high-latitude (32°–45°N, 40°–100°E) and low-latitude (5°–18°N, 40°–100°E) region are defined as the northern SAH mode index (N-SAHI) and the southern SAH mode index (S-SAHI), respectively.

To affirm the above definitions, a rotated EOF analysis (REOF) is then utilized to these two leading unrotated EOF modes and generate two leading rotated modes (Fig. 2c, d). REOF method is usually more statistically and physically reasonable and benefits to capture the regional characteristics (Horel 1981; Hannachi et al. 2007). The spatial pattern achieved through REOF is often simpler than that gained via EOF and may be better represent the regional characteristics (Horel 1981). There are many types of REOF projects (Richman 1986), and the most popular Varimax REOF analysis (Kaiser 1958) is applied in this study. The Kaiser varimax rotation is a common rotation performed on atmospheric or oceanographic data. Interestingly, the first two REOF modes display large and opposite loading regions over the mid- to high-latitude (30°–50°N) and low-latitude (0°–20°N) region, respectively (Fig. 2c, d). The percent of variance accounted by the first two modes are 37.4% and 30.7%, respectively,

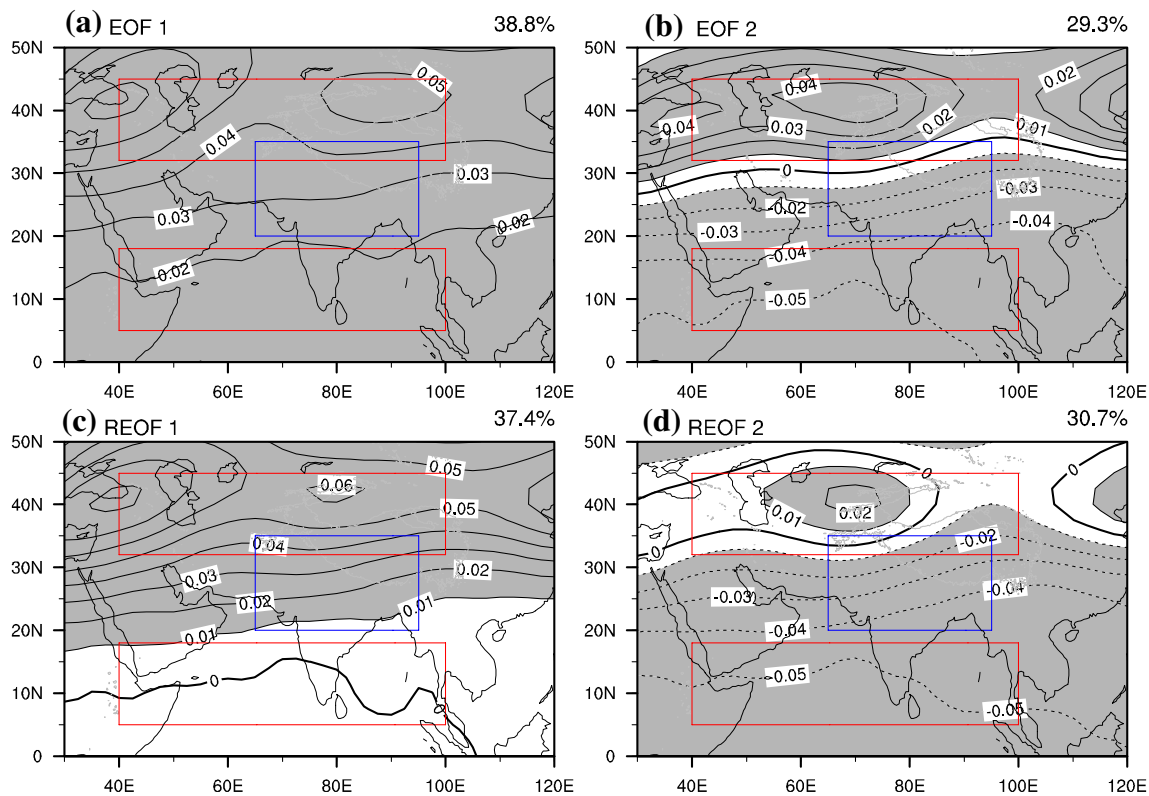


Fig. 2 The **a** first, **b** second EOF modes, and **c** first and **d** second rotated EOF mode of JJA HGT at 150-hPa over the region of (0° – 50° N, 30° – 120° E) for the period 1980–2017. Shading is applied for stressing purpose. The two red and blue boxes denote the regions

(32° – 45° N, 40° – 100° E), (5° – 18° N, 40° – 100° E) and (20° – 35° N, 65° – 95° E) used to define the N-SAH, S-SAH and E-SAH index, respectively

indicating that the HGT variations over the above-mentioned two regions are of equal importance. The correlation coefficients (CC) of the first two REOF modes is -0.20 (obtained by employing the two principal component time series), which reveals that the two modes are nearly independent.

Comparing Figs. 1 and 2, the largest loading region in Caspian Sea/northeastern China for the first two EOF modes (Fig. 2a, b), the maximum loading area in the first REOF mode (Fig. 2c), and the area with large standard deviation over the mid- to high-latitude region (Fig. 1b) almost cohere with each other. Analogously, the relatively large loading area over southern TP and Indian Ocean for the first two EOF modes (Fig. 2a, b), the maximum loading area for the second REOF mode (Fig. 2d), and the region with relatively strong standard deviation in Indian Ocean (Fig. 1b) are generally in accord with each other. Consequently, considering the climatological SAH location (Fig. 1a), it is reasonable to define area-average 150-hPa HGT over the regions of the mid-to high-latitude (32° – 45° N, 40° – 100° E) and low-latitude (5° – 18° N, 40° – 100° E) region as the N-SAHI and S-SAHI, respectively, to represent the variability of the southern and northern SAH mode. For comparing purpose, the area-mean of 150-hPa HGT over the region

of (20° – 35° N, 65° – 95° E), which regarded the SAH as an entirety in Zhang et al. (2005), is also utilized and termed as E-SAHI in this study.

In the follow analysis, we primarily pay attentions on interannual signals. The E-SAHI, N-SAHI, and S-SAHI have been subjected to 9-year running mean filtering analysis to remove the variation with period longer than 9 years (Fig. 3). As displayed in the picture, the three indices show remarkable interannual variabilities. The CC between N-SAHI and S-SAHI is 0.01, indicating that the interannual variations of the N-SAHI and S-SAHI is totally independent. The CC between N-SAHI (S-SAHI) and E-SAHI is 0.61 (0.62), exceeding 99% confidence level. Based on the ± 0.5 standard deviations of the three indices, 9 strong E-SAH years, 15 weak E-SAH years, 11 strong N-SAH years, 10 weak N-SAH years, 13 strong S-SAH years, and 14 weak S-SAH years during 1980–2017 were selected (see Table 2). As shown in Table 2, four strong years (1991, 1998, 2010, 2016) are simultaneously observed in strong N-SAH and S-SAH years, accounting for 4/11 and 4/13 of the corresponding group. Similarly, 2 weak years (1992, 2004) are also concurrently belong to the weak N-SAH and S-SAH years, accounting for 2/10 and 2/14, respectively. This further

confirms that the interannual variations of the N-SAH and S-SAH are nearly independent. 6 (7) out of 11 (13) strong N-SAHI (S-SAHI) years are simultaneously observed in strong E-SAH years, accounting for 6/11 (7/13). 6 (10) out of 10 (14) weak N-SAH (S-SAH) years are also seen in weak E-SAH years, accounting for 6/10 (10/14). This further confirms that the interannual variations of N-SAH and S-SAH are closely associated with those of the E-SAH.

To further confirm the reliability and ability of N-SAHI and S-SAHI depicting the SAH variations, several existing SAH indices which regarded SAH as an entirety are utilized in the following analysis. The details of these indices are introduced in Table 1. The CC among these SAH indices are displayed in Table 3. The N-SAHI and S-SAHI are closely associated with *I*area (0.59, 0.70), *I*inta (0.55, 0.57), *I*intb (0.55, 0.68), and *I*intc (0.60, 0.51), generally coincide with those for E-SAHI. Wei et al. (2012) defined the north–south shift index (termed as *I*sn) of SAH as the difference between area-average HGT over

(In 27.5°–32.5°N, 50°–105°E) and those averaged over (*I*s 22.5°–27.5°N, 50°–105°E). Accordingly, the CC between *I*n (*I*s, *I*sn) and those indices are also displayed in Table 3. *I*n (*I*s) are closely related to N-SAHI (S-SAHI) indices. Meanwhile, it should be noted that the CC between *I*n and *I*s is 0.68, indicating that they are not independent. *I*sn is weakly associated with *I*area (0.04), *I*inta (0.19), *I*intb (0.04), *I*intc (0.27), and E-SAHI (0.16), revealing that *I*sn can only present the north–south shift of the SAH, but is failure to depict the SAH strength variation. However, the N-SAHI and S-SAHI are prominently related to *I*sn, with 0.63 and –0.65 correlation coefficient, exceeding 99% confidence level. This indicates that the N-SAHI and S-SAHI cannot merely well depict variations of the SAH strength but also the meridional movement of the SAH.

We also perform an EOF, REOF, and standard deviation analysis for 150-hPa HGT over the corresponding regions based on ERA-Interim dataset, and the results are similar with those based on NCEP-NCAR reanalysis. Hence, the

Fig. 3 The normalized interannual time series of E-SAHI (black curve), N-SAHI (blue curve) and S-SAHI (red curve) on the period of 1980–2017

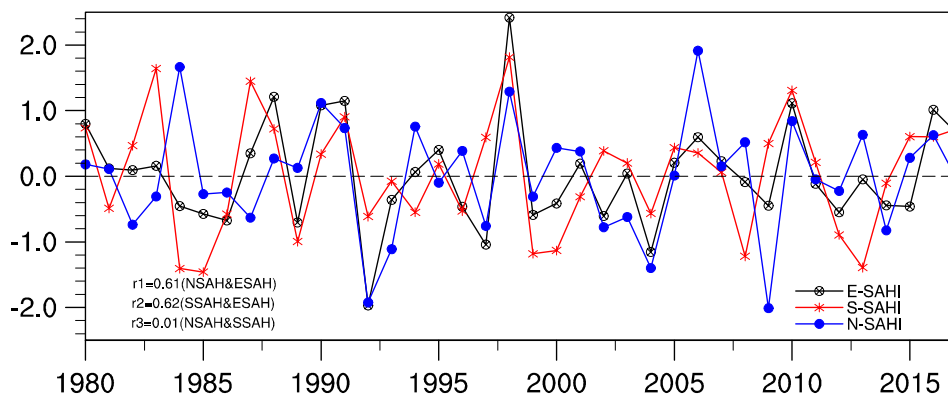


Table 2 List of strong and weak years of E-SAH, N-SAH and S-SAH for the period 1980–2017

	Strong	Weak
E-SAH	1980, 1988, 1990, 1991, 1998, 2006, 2010, 2016, 2017	1984, 1985, 1986, 1989, 1992, 1996, 1997, 1999, 2000, 2002, 2004, 2009, 2012, 2014, 2015
N-SAH	1984, 1990, 1991, 1994, 1998, 2000, 2006, 2008, 2010, 2013, 2016	1982, 1987, 1992, 1993, 1997, 2002, 2003, 2004, 2009, 2014
S-SAH	1980, 1982, 1983, 1987, 1988, 1991, 1997, 1998, 2009, 2010, 2015, 2016, 2017	1981, 1984, 1985, 1986, 1989, 1992, 1994, 1996, 1999, 2000, 2004, 2008, 2012, 2013

Table 3 Correlation coefficient (CC) between different SAH indices

	<i>I</i> area	<i>I</i> inta	<i>I</i> intb	<i>I</i> intc	E-SAHI	<i>I</i> n	<i>I</i> s	<i>I</i> sn
N-SAHI	0.59*	0.55*	0.55*	0.60*	0.61*	0.71*	0.20	0.63*
S-SAHI	0.70*	0.57*	0.68*	0.51*	0.62*	0.44*	0.95*	–0.65*
<i>I</i> n	0.92*	0.96*	0.93*	0.97*	0.97*	1.0	0.68*	0.36*
<i>I</i> s	0.86*	0.77*	0.86*	0.73*	0.81*	0.68*	1.0	–0.43*
<i>I</i> sn	0.04	0.19	0.04	0.27	0.16	0.36*	–0.43*	1.0

The symbol of “*” denotes that the CC exceeds the 95% confidence level

results based on NCEP-NCAR reanalysis are primarily discussed in the following study.

4 Interannual variations associated with the northern and southern mode

In this section, we perform the composite analyses to figure out the different features related to the E-SAH, N-SAH and S-SAH variations. Figure 4 displays the composite differences and the contour lines for 14,320 gpm of JJA 150-HGT for the strong and weak years of E-SAH, N-SAH and S-SAH (list in Table 1). For the E-SAH (Fig. 4a), the encircled range of the 14,320 gpm contour line are remarkably larger, and expand toward both meridional and zonal directions in strong E-SAH comparing to weak case. Remarkably positive differences between the strong and weak case are observed over the region of (0° – 40° N, 10° – 140° E), where the SAH generally exists. However, the strong N-SAH is located further north than those in the weak case, and positive differences are only remarkably observed over the mid- to high-latitude region (north of 25° N). Meanwhile, the strong S-SAH moves further southward than the weak case, and positive differences are only significantly observed over the low-latitude region (south of 25° N). Almost no significant differences are seen over the south of 25° N for N-SAH (north of 25° N for S-SAH), and no distinctly meridional movement appearing in the southern side for N-SAH (northern side for S-SAH).

Figure 5 displays the composite anomalies of 150-hPa HGT for strong and weak E-SAH, N-SAH, S-SAH cases. For the strong E-SAH cases (Fig. 5a), significantly positive anomalies cover over the low-latitude and mid- to high-latitude region, with five larger centers existing over the northern Atlantic Ocean, Turkey, the north of TP, southern Japan, and southern America, respectively. Similarly, negative anomalies are remarkably observed over the southern Asia and Africa in the weak E-SAH cases, except that no significant anomalies appear over the north of 40° N, tropical Indian Ocean and tropical Pacific. However, different anomalies patterns are obviously observed in the N-SAH and S-SAH cases (Fig. 5c, d). Positive (negative) anomalies are significantly observed over north of 30° N, with larger centers exceeding 20 gpm existing over Atlantic, the Caspian Sea, northeastern China, and Kuril Islands in strong (weak) N-SAH cases, which is especially similar with the pattern of the circumglobal teleconnection (CGT). No significant anomalies occur over the low-latitude and tropical region. For the S-SAH, positive (negative) anomalies are remarkably observed over south of 30° N for the strong (weak) S-SAH cases. Accordingly, the 150-hPa HGT anomalies distributions for E-SAH, N-SAH, and S-SAH are obviously different. The anomalies associated

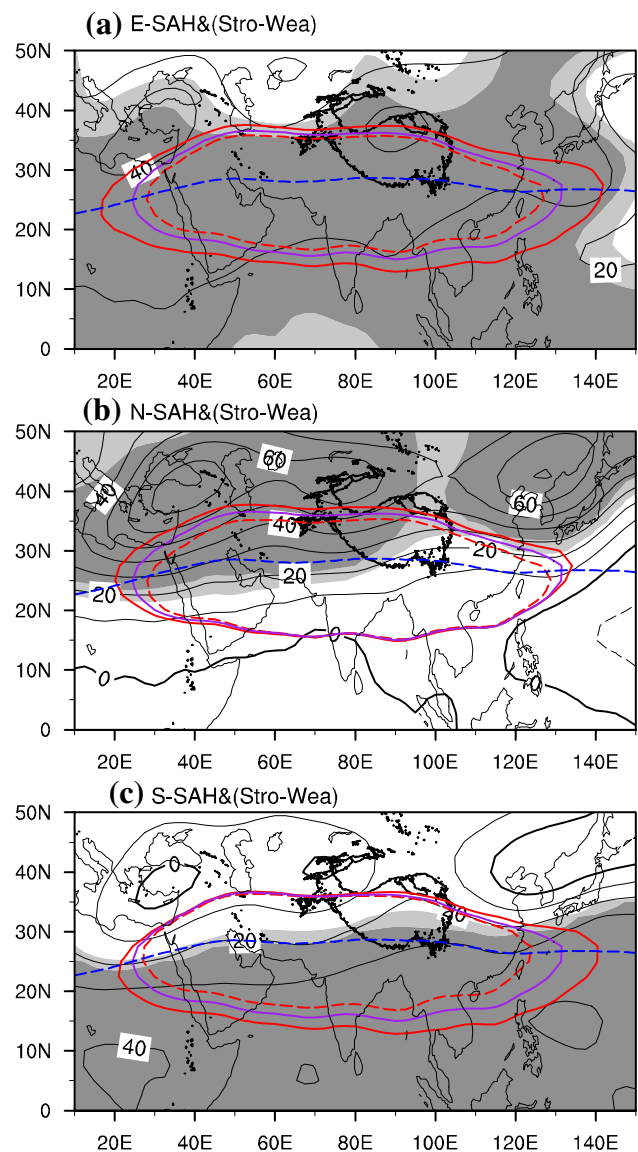


Fig. 4 Composite differences of 150-HGT in JJA between the strong and weak mode of **a** E-SAH, **b** N-SAH, **c** S-SAH. Shadings indicate the composite differences exceeding the 95% significance level. Contour in thick black denotes the Tibetan Plateau region with topography exceeding 3000 m. Climatological JJA 14,320-gpm contours are indicated by purple contours. Red solid and dashed lines denote the 14,320-gpm contours of the strong and weak mode in **a–c**. Blue dashed line denotes the ridge line of the SAH where the climatological JJA zonal wind equals zero

with E-SAH variability cover larger regions including the low-latitude and mid- to high-latitude region. However, those related to N-SAH (S-SAH) are limited over the mid- to high-latitude (low-latitude) region. The distribution of HGT anomalies related with the N-SAH and S-SAH are inconsistent with those in E-SAH which regarded the SAH as an entirety in numerous previous studies.

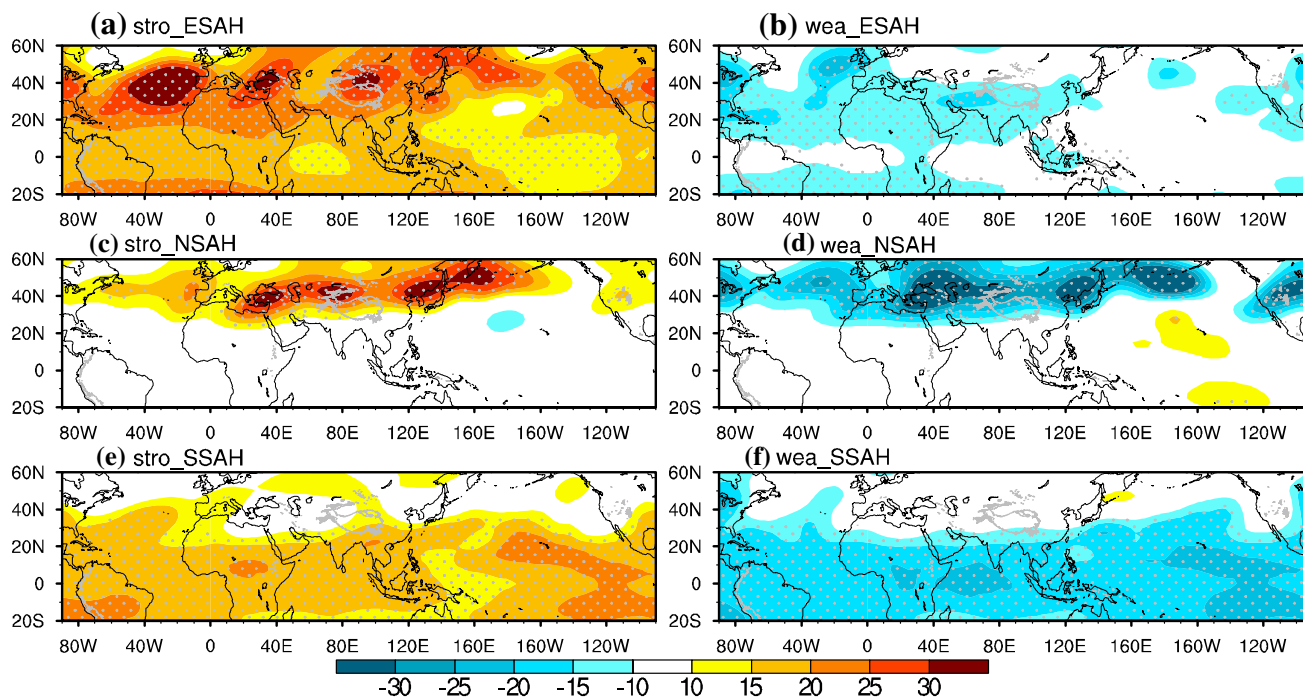


Fig. 5 Composite anomalies of 150-HGT (units: gpm) for different cases listed in Table 1. Contour in gray denotes the Tibetan Plateau region with topography exceeding 3000 m. Stippled areas indicate

that the anomalies are significantly at 90% confidence level according to the Student's *t* test

Figure 6 displays the HGT anomalies averaged over 40°–100°E for E-SAH, N-SAH, S-SAH variabilities. For strong E-SAH case, positive anomalies are prominently observed from low latitude to mid-high latitude above 500 hPa level. Negative anomalies are obviously seen in 10°–35°N above 400 hPa level in weaker E-SAH years. Nevertheless, for the N-SAH, the positive (negative) anomalies are obviously observed over north of 30°N region above 400 hPa, with a largest center existing in 42°N at 150 hPa level in strong (weak) N-SAH case. Meanwhile, positive (negative) anomalies are limited to south of 30°N in the strong (weak) S-SAH. It is noted that the anomalies associated with S-SAH are observed above 700 hPa level, which is lower than those in the N-SAH (400 hPa). This further confirms that the HGT anomalies related to E-SAH variability expand along low latitude to mid-high latitude, whereas those related to N-SAH (S-SAH) are only limited to the mid-high latitude (low latitude).

Previous researches have demonstrated that SAH variation is closely associated with the tropospheric temperature (TT) over the tropics and southern TP regions (Huang et al. 2011; Qu and Huang 2012; Xue et al. 2015). Based on previous studies, TT is defined as the average of air temperature from 1000 hPa to 150 hPa. Figure 7 shows the anomalies of TT and zonal wind at 150 hPa connected with E-SAH, N-SAH, and S-SAH. For strong E-SAH, positive TT anomalies are concurrently observed over low and

mid-high latitude (Fig. 7a), with five larger centers occurring over the Atlantic, Caspian Sea, northern TP, Japan, and America. Easterly wind anomalies exist over Africa and western Indian Ocean, and no obvious wind anomalies appear over Asia region. Negative TT anomalies are observed over the Atlantic, Indian Ocean, and TP regions for the weak E-SAH cases. However, for strong (weak) N-SAH, positive (negative) TT anomalies are remarkably seen over the mid- to high-latitude region. Westerlies (easterlies) over the Caspian Sea regions and easterlies (westerlies) anomalies over southern Asia/northwestern Pacific are concurrently observed in strong (weak) N-SAH case, respectively. Summertime upper tropospheric westerlies lie in the northern flank of the SAH (north of 30°N), and easterlies situate in the southern flank of the SAH (south of 27°N) (Wei et al. 2017, Fig. 1). The westerly (easterly) anomalies over the Caspian Sea and easterly (westerly) anomalies over southern Asia/northwestern Pacific strengthen (weaken) the total westerly over mid-latitude region and easterly over low-latitude region, then induce a stronger (weaker) N-SAH anticyclonic circulation here, accompanied by shifting further northward (southward) in the north side of N-SAH. Simultaneously, for the strong (weak) S-SAH cases, positive (negative) TT and westerly (easterly) anomalies are obviously seen over the low-latitude region. The westerly (easterly) anomalies covering around 20°N weaken (strengthen) the climatological

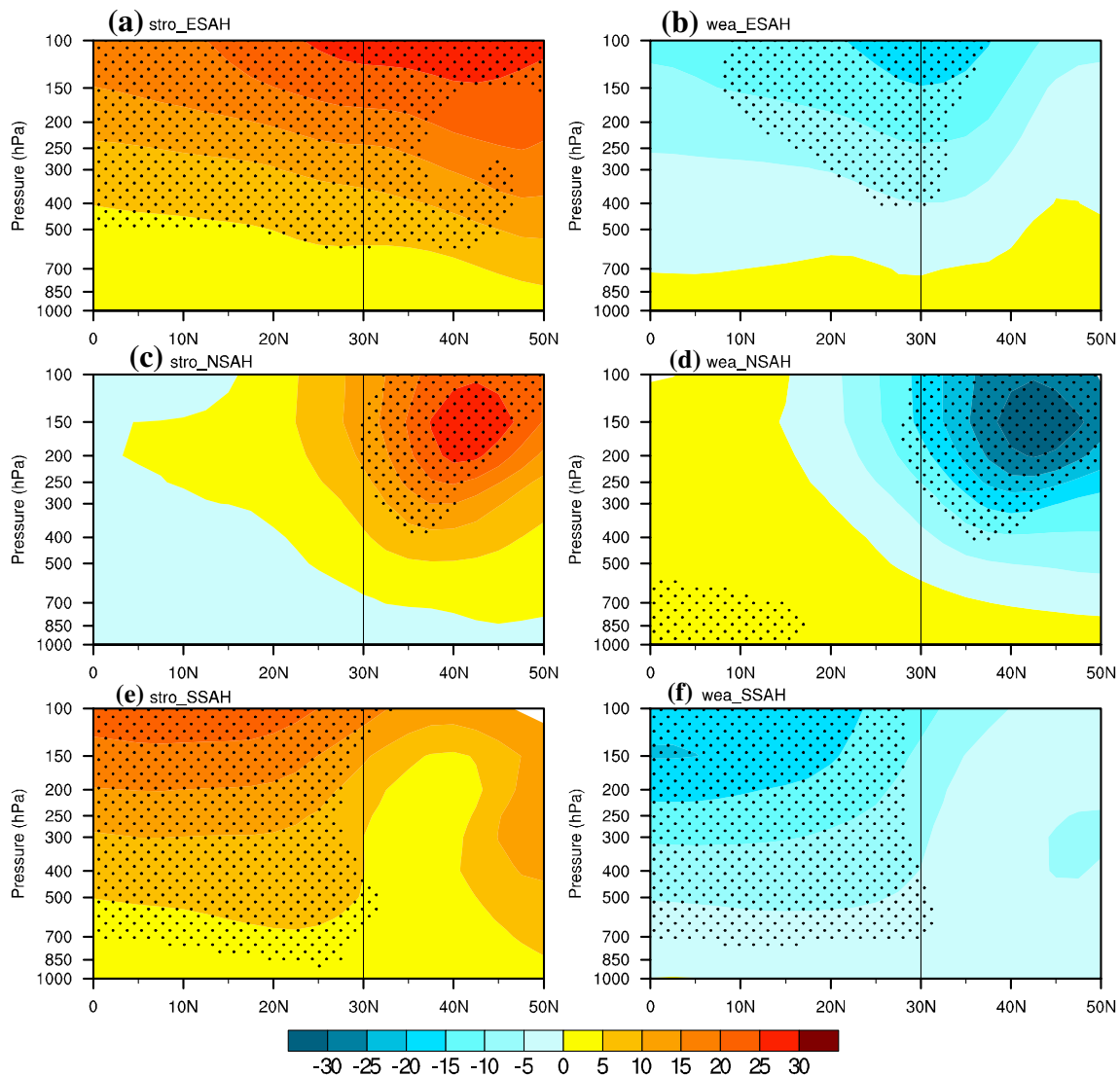


Fig. 6 Composite anomalies of HGT (units: gpm) (40° – 100° E) for different cases listed in Table 1. Stippled areas indicate that the anomalies are significantly at 90% confidence level according to the Student's t test. The black vertical line denotes 30° N

easterlies jet stream, and form a stronger (weaker) S-SAH anticyclonic circulation here. No significant wind anomalies are observed over mid- to high-latitude region for the S-SAH case. Figure 8 displays the air temperature anomalies averaged over 40° – 100° E associated with E-SAH, N-SAH, S-SAH variability. Similarly, positive (negative) air temperature anomalies emerge over 0° – 35° N above 400 hPa in strong (weak) E-SAH cases. However, positive (negative) anomalies are obviously observed over mid- to high-latitude region above 600 hPa, with maximum center situated in 45° N at 250 hPa level in strong (weak) N-SAH cases. For S-SAH, the air temperature anomalies are mainly limited to low-latitude region from the surface to 150 hPa. The distribution of TT and air temperature

anomalies are in accordance with those in HGT fields (Figs. 5, 6).

Accordingly, when the SAH is regarded as an entirety based on previous studies, it strengthens distinctly and expands toward meridional and zonal directions in strong E-SAH case comparing to weak E-SAH. The variations of HGT and TT anomalies related to E-SAH are concurrently observed over the low-latitude and mid- to high-latitude region. By contrast, when the northern and southern mode of the SAH are defined in this study, some innovative and different findings are uncovered. For instance, the HGT and TT anomalies are only distinctly strengthened (weakened) over the northern side of N-SAH, and only the northern side of N-SAH expands northward (southward) in strong (weak)

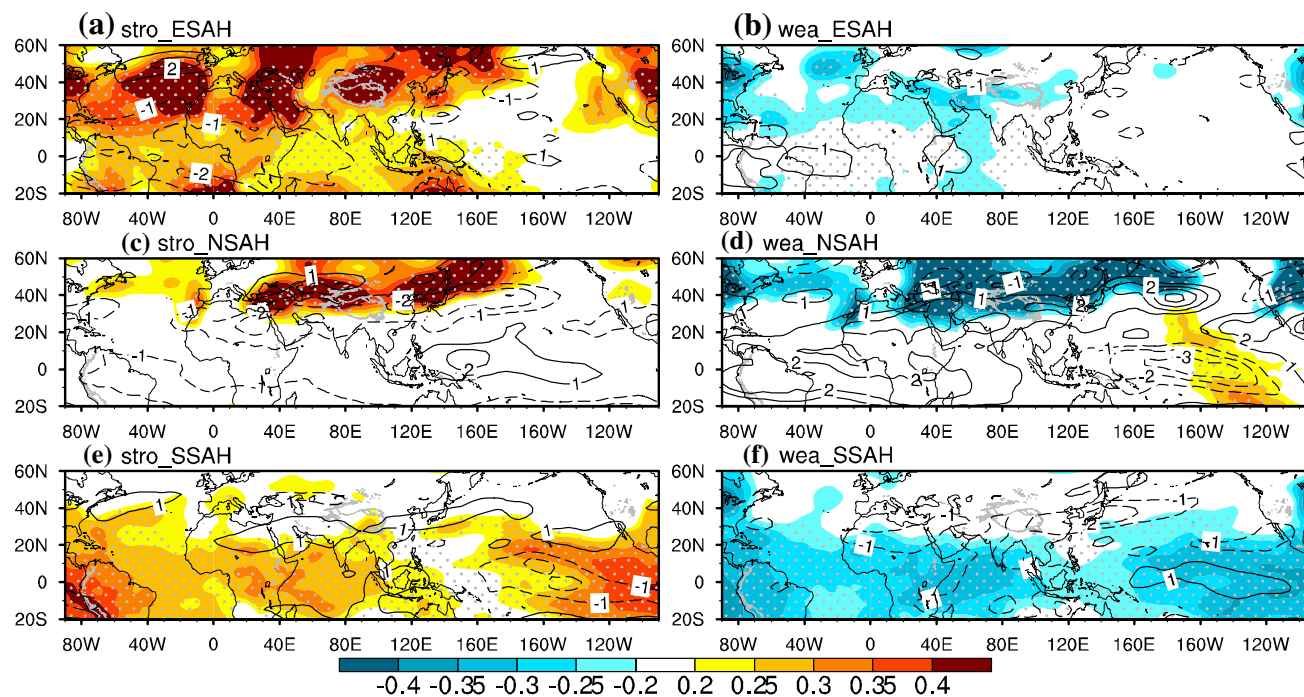


Fig. 7 Same as Fig. 5, but for tropospheric temperature (air temperature averaged from 1000 to 150 hPa, unit: °C). Contour in black denotes the zonal wind anomalies at 150 hPa

N-SAH case. Westerlies (easterlies) over the Caspian Sea regions and easterlies (westerlies) anomalies over southern Asia/northwestern Pacific are concurrently observed in strong (weak) N-SAH case, respectively. No distinct anomalies occur over the southern side of N-SAH. Anomalous HGT (TT) differences between strong and weak N-SAH are limited to the mid-high latitude (north of 30°N). On the contrary, The HGT and TT anomalies are only strengthened (weakened) obviously over the southern side of S-SAH, and only the southern side of S-SAH shifts southward (northward) in the strong (weak) S-SAH case. Nearly no remarkable variations are observed over the northern side of S-SAH. Anomalous HGT (TT) differences between strong and weak S-SAH are only observed over low-latitude (south of 25°N) region. According to the above results, the variation features associated with N-SAH and S-SAH are distinctly different and independent, indicating that it is necessary and of scientific significance to distinguish the northern and southern mode of the SAH.

5 Possible impacted factors of the northern and southern mode of the SAH

5.1 Rainfall anomalies and meridional circulation

The SAH is a thermal high-pressure and its center has the property of heat preference, generally situating over or

shifting toward a region with relative larger heating rates (Qian et al. 2002). Previous studies suggested that the formation of SAH is attributed to the summertime continental heating primarily including surface sensible heat flux associated with TP and latent heat release related to Asian monsoon (Flohn 1957, 1960; Mason and Anderson 1963; Tao and Zhu 1964; Krishnamurti et al. 1973; Zhang et al. 2002; Liu et al. 2004; Wu et al. 2016). The position and extension of SAH usually reveal thermodynamic anomalies on land and atmosphere. Hence, it is of great significance to explore thermodynamic factors impacting SAH variabilities. To determine the latent heat forcing source related to summer monsoon rainfall of E-SAH, N-SAH, and S-SAH, the composite anomalies of summer precipitation anomalies from CRU data are investigated in Fig. 9. For strong E-SAH case, significant positive precipitation anomalies are presented over western Indian Peninsula. Simultaneously, weak positive anomalies exist over northern Indian Peninsula, central and northeastern China. The anomalies distribution associated with weak E-SAH are nearly out of phase with strong E-SAH. In contrast, the positive (negative) anomalies over India Peninsula and northeastern China associated with strong (weak) N-SAH are significantly strengthened, indicating a stronger (weaker) summer rainfall anomalies related to N-SAH. Furthermore, for the S-SAH cases, the precipitation anomalies over India Peninsula and northeastern China are weakened. Significant positive (negative) anomalies are seen over central China (east of TP) in the strong S-SAH.

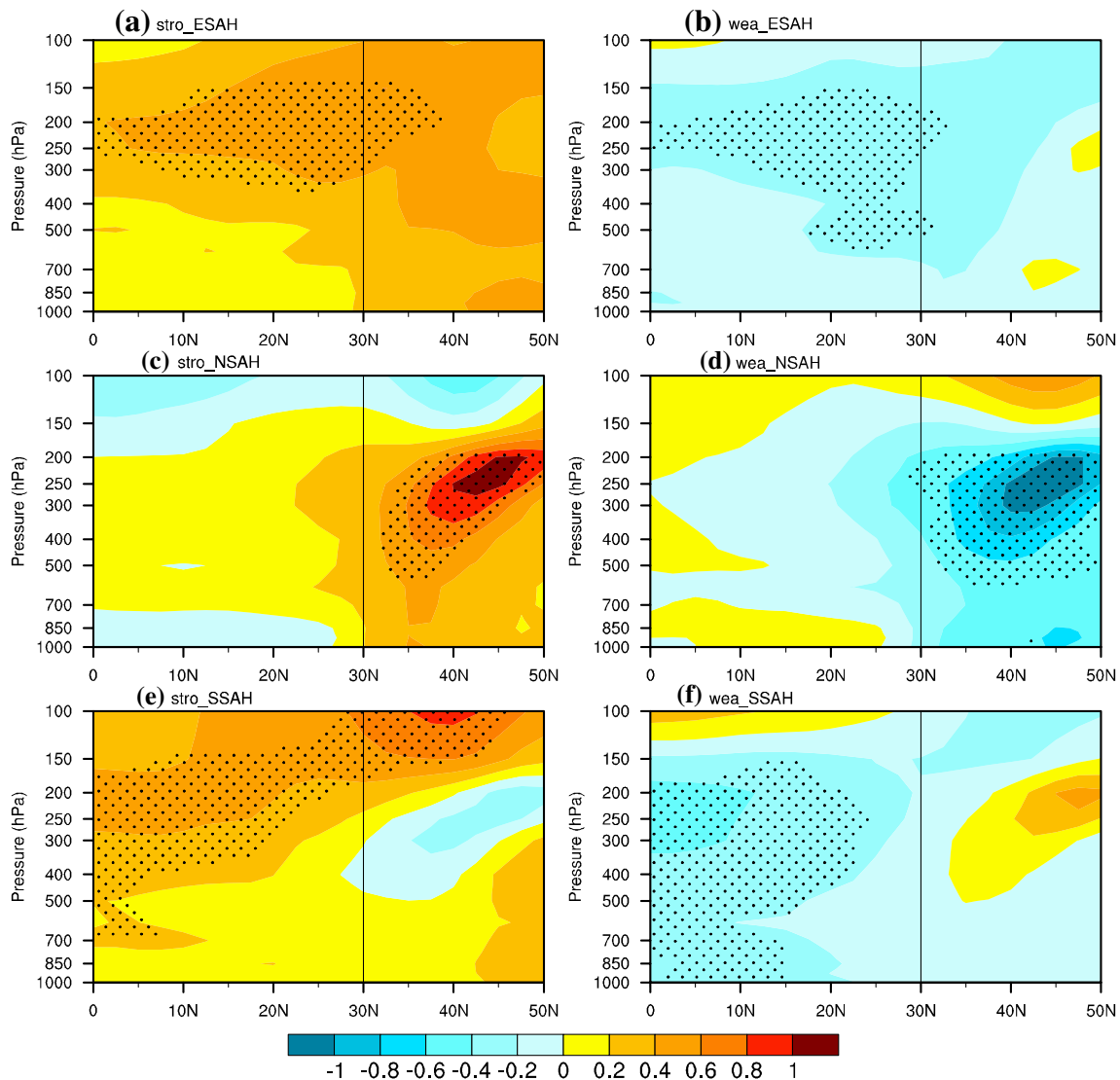


Fig. 8 Same as in Fig. 6, but for tropospheric temperature (unit: °C)

Accordingly, based on the distribution of precipitation anomalies associated with E-SAH, N-SAH, and S-SAH, prominent precipitation differences are identified over the Indian Peninsula. Figure 10 displays the meridional profile (40° – 100° E) of the composite flow, vertical velocity and air temperature anomalies associated with E-SAH, N-SAH, and S-SAH. The composite flow reveals that strong ascending (descending) motion exists over south of 38° N (38° – 50° N) in strong E-SAH, and strong descending motion along nearly 0° – 50° N associated with weak E-SAH. The vertical velocity difference between strong and weak E-SAH exhibit significant ascending motion over south of 35° N. Similar to Fig. 8a, b, there is a significant positive air temperature center in the middle-upper troposphere (500–200 hPa) over TP (25° – 35° N). By contrast, for the strong N-SAH, the ascending motion

strengthens and is located over southern TP (25° – 35° N), and the descending motion over northern TP expands to upper troposphere. The distribution of meridional flow and vertical velocity in the weak N-SAH is nearly out of phase with strong N-SAH, accompanied by a strong descending motion over southern TP and ascending motion over northern TP. The vertical velocity difference (Fig. 10f) demonstrate a remarkably strong meridional circulation along 20° – 50° N. Similar to Fig. 8c, d, a remarkable positive warming center is observed over mid-upper troposphere (500–200 hPa) over northern TP (north of 35° N). The rainfall over Indian Peninsula is more than normal (Fig. 9c), and the strong ascending motion over southern TP (25° – 35° N) further enhances the latent heat of condensation (figure not shown). This increasing of latent heat of condensation finally contribute to increasing air

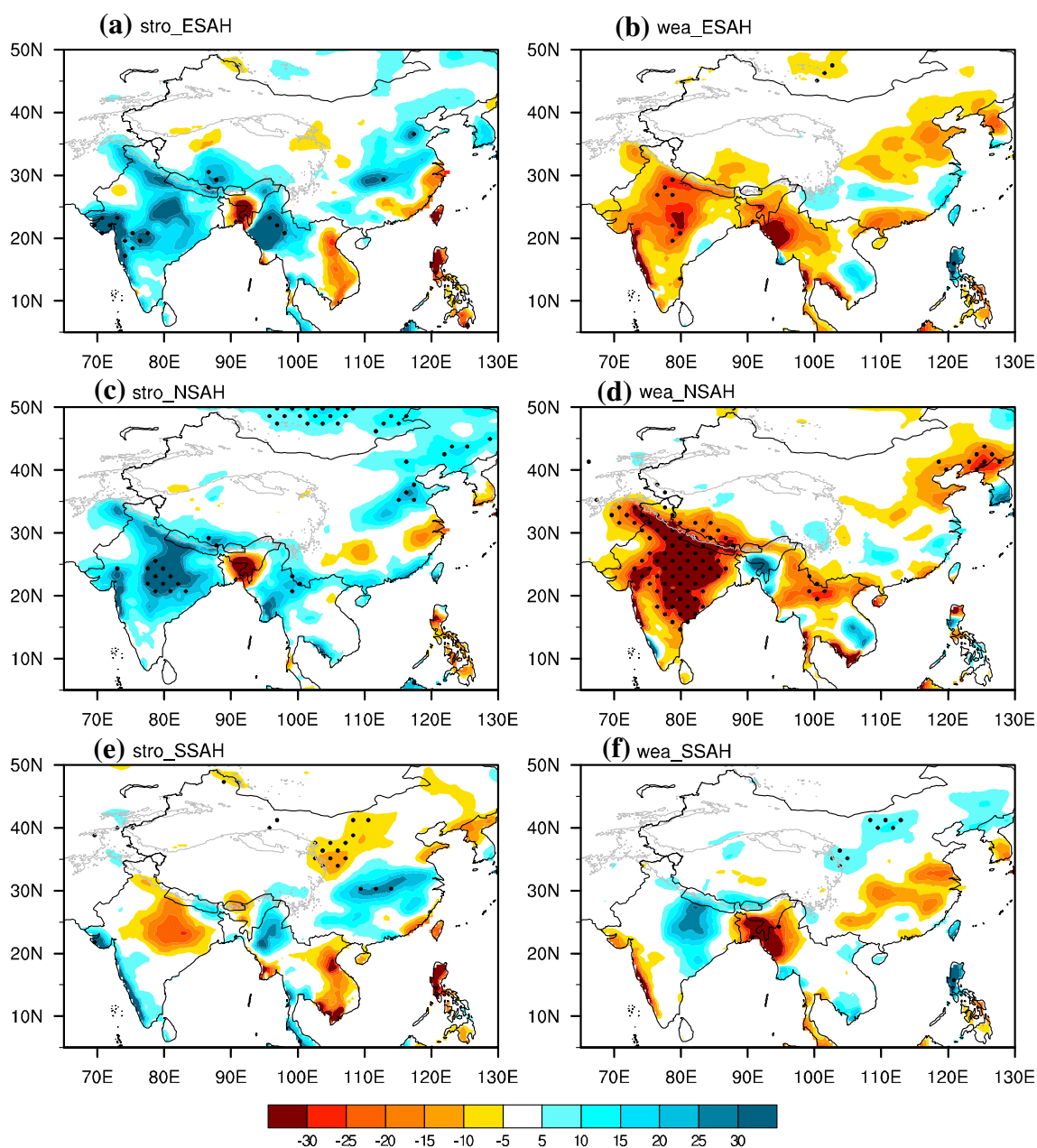


Fig. 9 Same as Fig. 5, but for precipitation (Unit: mm/month)

temperature locally in the middle-upper troposphere. Furthermore, the descending motion over northern TP (north of 35°N) also leads to warm center in low-middle troposphere here through air adiabatic compression. The ascending and descending motion regions associated with N-SAH all extend to further north comparing to E-SAH, which indicates a northward shift in the eddy. Accordingly, the anomalies associated with N-SAH prefer to exist over north of 30°N based on its property of heat preference with a warming center over north of 35°N (Fig. 10f). By

contrast, for the strong S-SAH, an ascending (descending) motion is located over south of 22°N (north of 22°N). The distribution of flow and vertical velocity in weak S-SAH is nearly out of phase with strong S-SAH. The difference of vertical velocity and air temperature (Fig. 10i) demonstrated a meridional circulation over southern TP (south of 32°N), which indicates a southward shift in the circulation comparing to N-SAH. However, the rainfall anomalies over Indian Peninsula associated with S-SAH is weak, indicating that there is other factor, for instance the tropical SST anomalies, accounting for the variation of S-SAH.

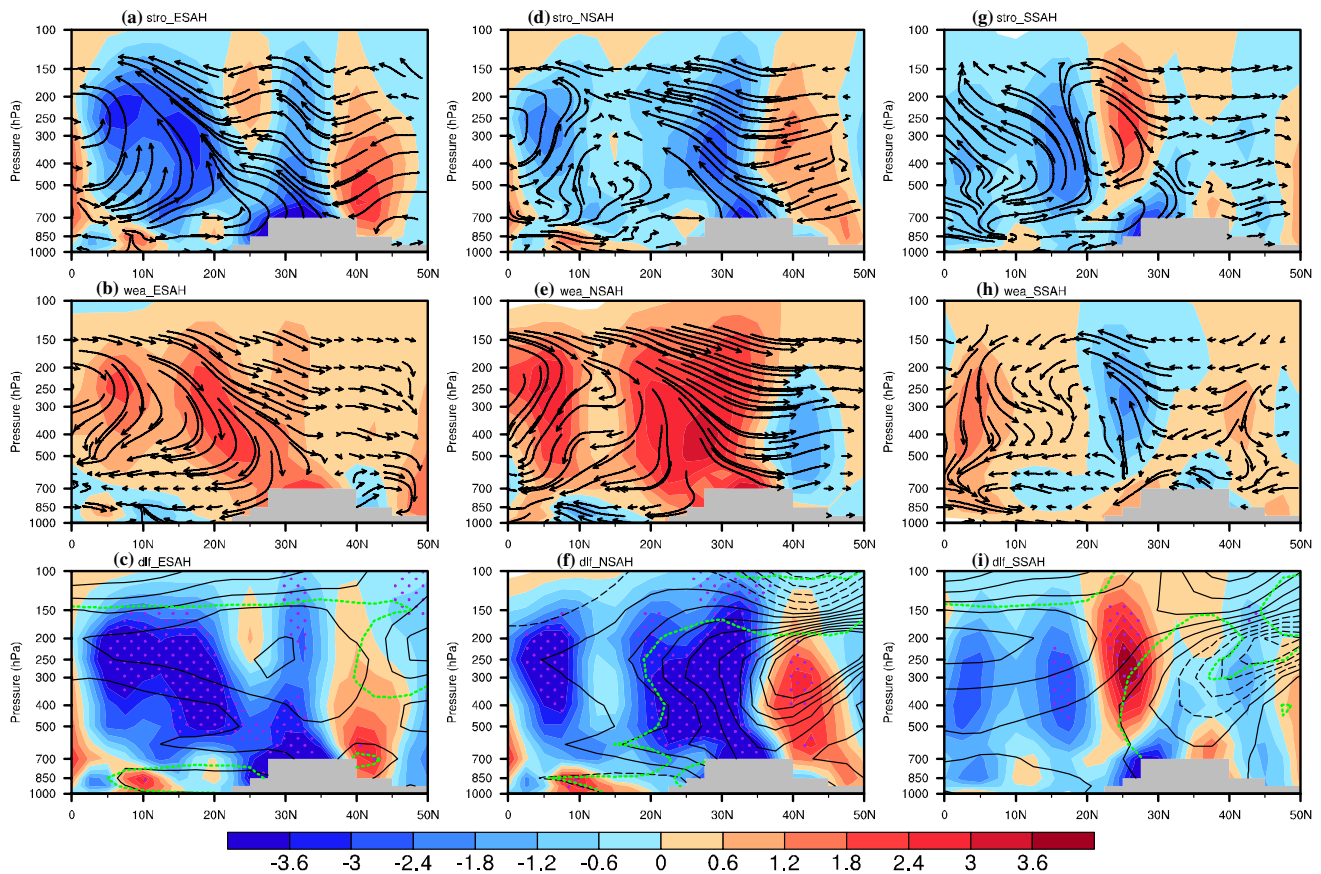


Fig. 10 Distributions of the flow field along 40° – 100° E (arrow lines) and vertical velocity (ω , unit: 10^{-3} Pa/s) for different cases listed in Table 1 (a, b, d, e, g, h). Positive anomalies (thick lines) and negative anomalies (dashed lines) of air temperature (unit: $^{\circ}$ C) and the strong-minus-weak ω values are displayed (c, f, i). A profile of

the terrain is shown at the bottom of each panel. Purple stippled areas and green dashed lines (c, f, i) indicate that the ω and air temperature differences are significantly at 90% confidence level according to the Student's t test

5.2 Land surface temperature

The rainfall anomalies and meridional circulation may exert impacts on the land surface temperature (LST) through cloud-radiation feedback. Thus, the composite anomalies of summer LST associated with E-SAH, N-SAH and S-SAH are presented in Fig. 11. For strong E-SAH case, four warm centers are identified over eastern America, the Caspian Sea, northeastern TP, eastern Okhotsk Sea, respectively. The cold anomalies in weak E-SAH case are weak and insignificant. It is noted that nearly no obvious anomalies exist over the Indian Peninsular in strong and weak E-SAH. By contrast, for strong N-SAH case, warm centers are obviously identified over northern TP, eastern China, and eastern Canada, respectively. Simultaneously, cold center is obviously identified over Indian Peninsula, which is caused by the cloud-radiation feedback due to strong rainfall and ascending motion here (Fig. 9c). The ascending motion over southern TP (Fig. 10d, 20° – 35° N) and heavy precipitation over Indian Peninsula may lead to increasing in cloud cover, which result

in less solar radiation down to surface, and then reduce the land surface temperature here. Meanwhile, the descending motion over northern TP (Fig. 10d) contributes to the warm centers over northern TP. For weak N-SAH case, cold anomalies almost control the mid- to high-latitude region (north of 30° N) with larger centers over the Caspian Sea, northern TP, eastern China, and America, respectively. Significantly warm centers are identified over Indian Peninsular and central Africa. The less rainfall over Indian Peninsula (Fig. 9d) and strong descending motion over southern TP (Fig. 10e) reduce the cloud cover here, leading to that more solar radiation reaches to the ground and increase the surface land temperature locally. Accordingly, prominent meridional LST gradient are obviously observed between the low latitude (7° – 30° N) and middle latitude (35° – 45° N). Furthermore, warm (cold) anomalies are obviously observed over tropical regions including northern South America, central Africa, Indian Peninsula, Indo China Peninsula, and Australia for the strong (weak) S-SAH case. No remarkable LST anomalies are observed over TP regions.

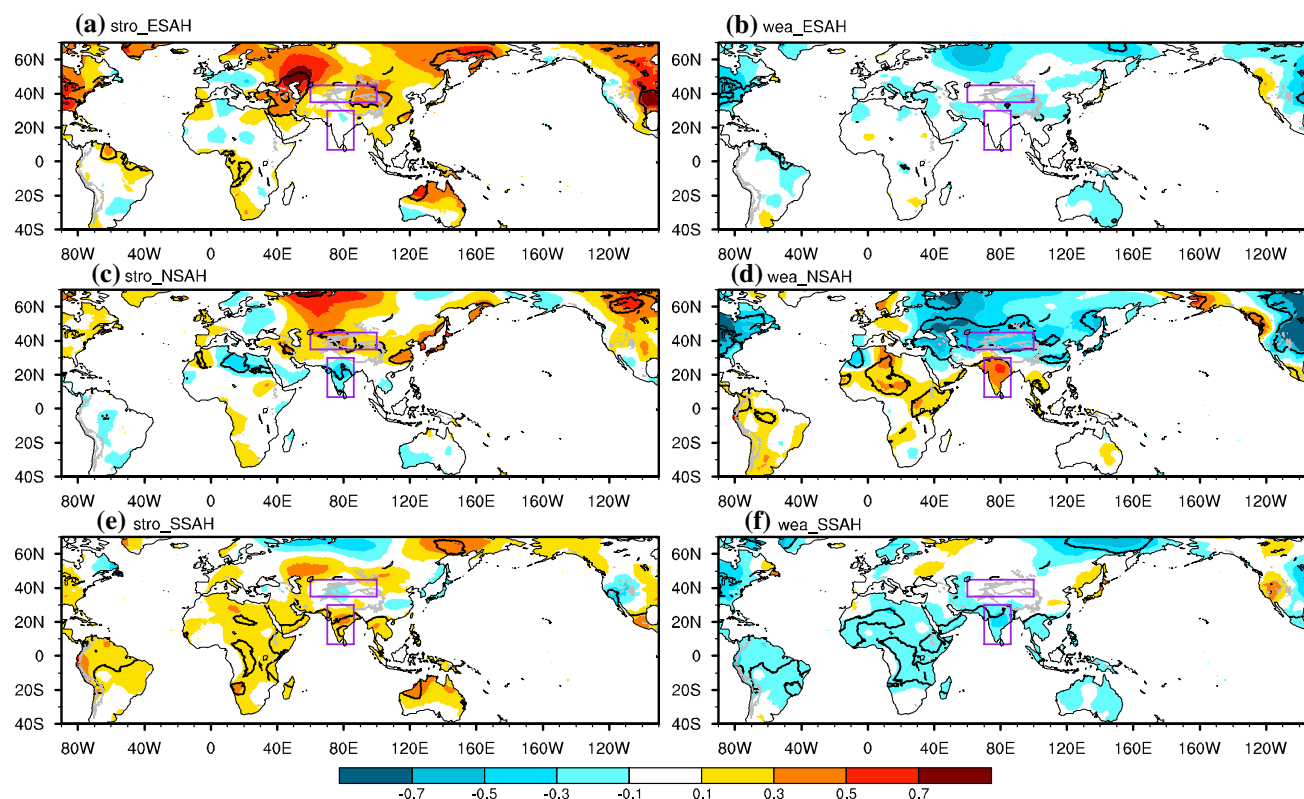


Fig. 11 Same as in Fig. 5, but for land surface temperature (LST, unit: °C, shading). Thick black lines indicate that the anomalies are significantly at 90% confidence level based on the Student's *t* test.

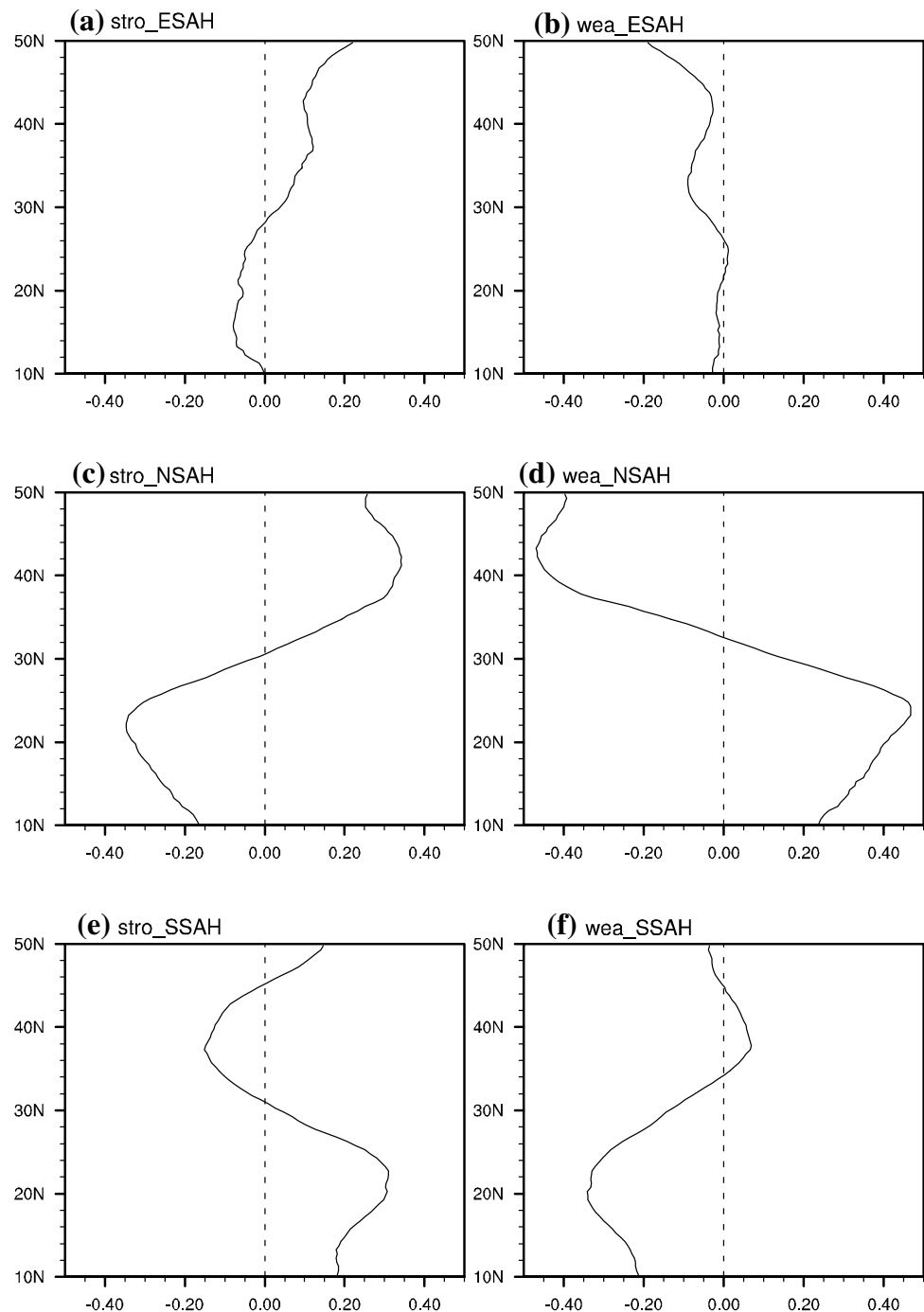
Accordingly, based on the distribution of LST anomalies associated with E-SAH, N-SAH, and S-SAH, prominent differences are identified over the TP and Indian Peninsula regions. Figure 12 displays the zonal mean LST anomalies averaged over 70°–86°E for strong and weak E-SAH, N-SAH, and S-SAH case. For strong E-SAH, the northern TP (32°–50°N, 70°–86°E) features warm LST anomalies, and Indian Peninsula (10°–30°N, 70°–86°E) features weak cold anomalies, which may result in a weak temperature meridional gradient here. For weak E-SAH, weak negative temperature exists over the northern TP, and no significant anomalies appear over Indian Peninsula. By contrast, for strong N-SAH case, dramatically warm (maximum greater than 0.3 °C) and cold anomalies (minimum less than –0.3 °C) are identified over the northern TP (30°–50°N, 70°–86°E) and Indian Peninsula (10°–30°N, 70°–86°E), respectively, resulting in a strong meridional LST gradient in a southward direction. For weak N-SAH, similar but opposite LST anomalies with cold signals (minimum less than –0.4 °C) over the northern TP and warm anomalies (maximum greater than 0.4 °C) over Indian Peninsula are obviously identified, respectively. This leads to a meridional LST gradient with a northward direction here. The phenomena illustrate the N-SAH variation is closely associated

The two purple boxes denote the regions of northern Tibetan Plateau (TP, 35°–45°N, 60°–100°E) and Indian Peninsula (7°–30°N, 70°–86°E) applied to calculate the regional mean LST, respectively

with the strong meridional gradient between northern TP and Indian Peninsula. Additionally, for S-SAH, the LST anomalies over the northern TP and Indian Peninsula are relatively weaker than those related to N-SAH, which result in a weaker meridional LST gradient. It is noted that LST anomalies over Indian Peninsula is obviously stronger than those in northern TP, indicating that S-SAH is closely associated with the LST anomalies over Indian Peninsula.

The LST anomalies associated with E-SAH, N-SAH, and S-SAH variations in Figs. 11 and 12 exhibit totally different features. To further investigate the relationships between LST anomalies with E-SAH, N-SAH, and S-SAH variations, the scatter plots between E-SAH (N-SAH, and S-SAH) and the LST anomalies averaged over mid-latitude northern TP (NTP, 35°–45°N, 60°–100°E), low-latitude Indian Peninsula (IND, 7°–30°N, 70°–86°E), and the difference between the two regions (DIF) are displayed in Fig. 13. It is found that the E-SAH variations are closely related to the LST anomalies over the northern TP with CC 0.41, exceeding 95% confidence level. The LST anomalies over Indian Peninsula and the DIF are weak related to E-SAH variations. However, the N-SAH variations are closely connected to the LST anomalies over the northern TP and Indian Peninsula, with CC 0.74

Fig. 12 Zonal mean LST anomalies in key region (70° – 86° E) for **a** Strong E-SAH, **b** weak E-SAH, **c** strong N-SAH, **d** weak N-SAH, **e** strong S-SAH and **f** weak S-SAH



and -0.50 , respectively, both far outstripping 99% confidence level. Simultaneously, the meridional LST gradient (DIF) are also closely positively connected to the N-SAH variations (with CC 0.70). Additionally, the S-SAH variations are closely related to the LST anomalies over the Indian Peninsula (with CC 0.62) and weakly connected to the LST anomalies over the northern TP (with CC 0.06). The meridional LST gradient is negatively connected to S-SAH, which may be caused by the LST anomalies over Indian Peninsula. Accordingly, the N-SAH variations are

closely connected to the LST anomalies over the northern TP, Indian Peninsula, and the meridional LST gradient between the northern TP and Indian Peninsula. The LST gradient from northern TP to Indian Peninsula associated with strong N-SAH will reduce the climatological surface temperature gradient from south to north, which widens wave movement and strengthens the northward meridional circulation (Fig. 10d, e), then results in significant warm air temperature center and strong N-SAH over mid-upper troposphere. By contrast, the E-SAH and S-SAH

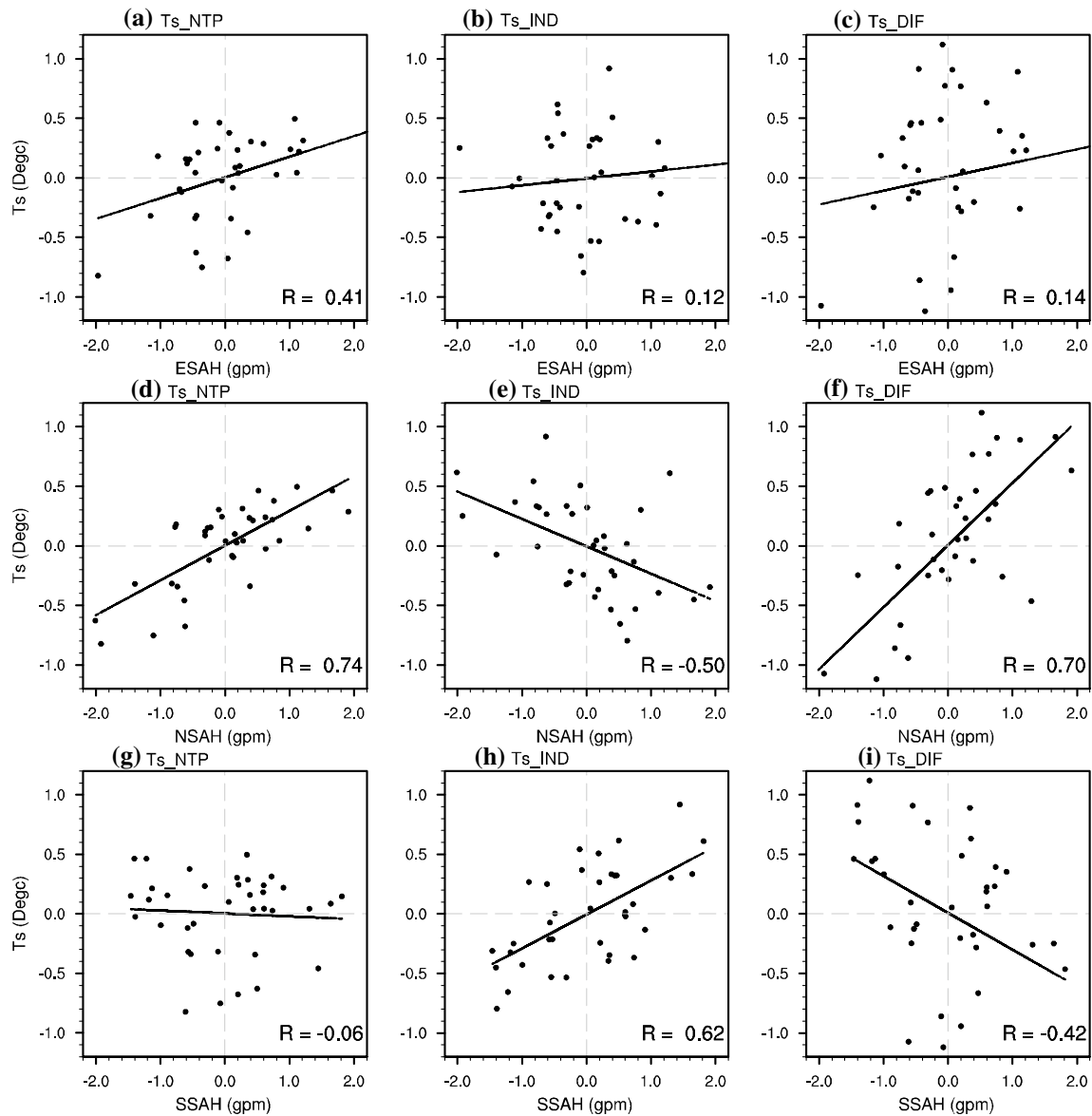


Fig. 13 Scatter plot between E-SAH and the averaged LST over a northern Tibetan Plateau (NTP, 35°–45°N, 60°–100°E), **b** Indian Peninsula (IND, 7°–30°N, 70°–86°E), and **c** difference of average LST over NTP and IND (DIF). **d–f** and **g–i** are same as **a–c**, but for

N-SAH and S-SAH case, respectively. Lines denote the best linear fitting. Correlation coefficients between E-SAH (N-SAH, S-SAH) and the averaged LST over NTP (IND) and DIF are shown in the lower right corner of corresponding picture, respectively

are closely related to LST anomalies over the northern TP and Indian Peninsula, respectively. Furthermore, the evolution of meridional distribution of the anomalies zonal-averaged LST over (40°–100°E), and corresponding strong (weak) years of N-SAH and S-SAH (labelled as S and W, respectively) are presented in Fig. 14. The strong N-SAH is generally accompanied by a warm center over northern TP, cold anomalies over Indian Peninsula, and meridional LST gradient from north to south, for instance, the year 1984, 1990, 1991, 1994, 2000, 2006, 2008, 2013, 2016. The weak N-SAH appears with cold northern TP, warm Indian Peninsular, and a meridional LST gradient from

south to north, such as the year 1982, 1987, 1992, 1993, 2002, 2003, 2004, 2009, 2014. Interestingly, one strong event in 1998 is accompanied by warm anomalies simultaneously existing over northern TP and Indian Peninsula, which may be caused by the strong El Niño events. Additionally, the strong (weak) S-SAH generally occurs with warm (cold) anomalies over Indian Peninsula, for instance, the year 1982, 1983, 1987, 1988, 1991, 1997, 1998, 2009, 2015 (1981, 1984, 1985, 1989, 1994, 1996, 1999, 2000, 2001, 2008, 2012, 2013). Several events such as 1980, 1986, 1992, 2010 cannot well match with the LST anomalies over corresponding regions, indicating that there are

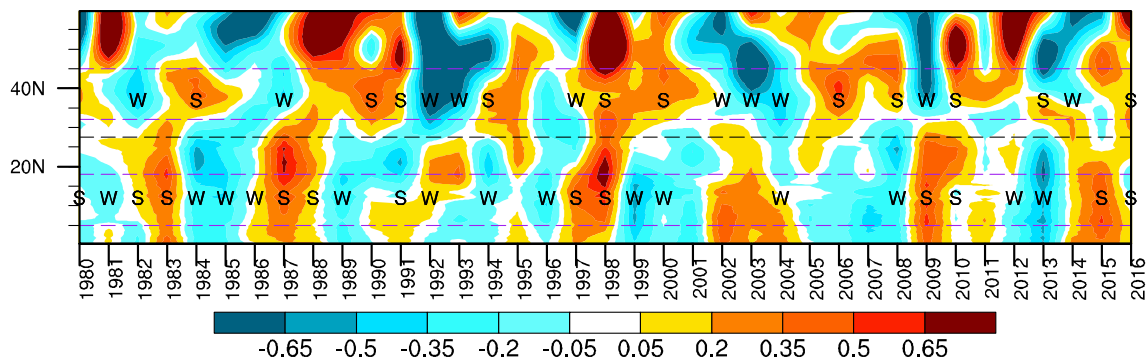


Fig. 14 The evolution of meridional distribution of the LST anomalies averaged over (40°–100°E), the strong (weak) N-SAH and S-SAH are labelled as W (S) over northern, and southern area,

respectively. The purple lines denote the latitude (32°–45°N), and (5°–18°N) applied to define N-SAH and S-SAH, respectively

other impacted factors contributes to N-SAH, S-SAH variations, which need be investigated in further research.

5.3 The circumglobal teleconnection (CGT)

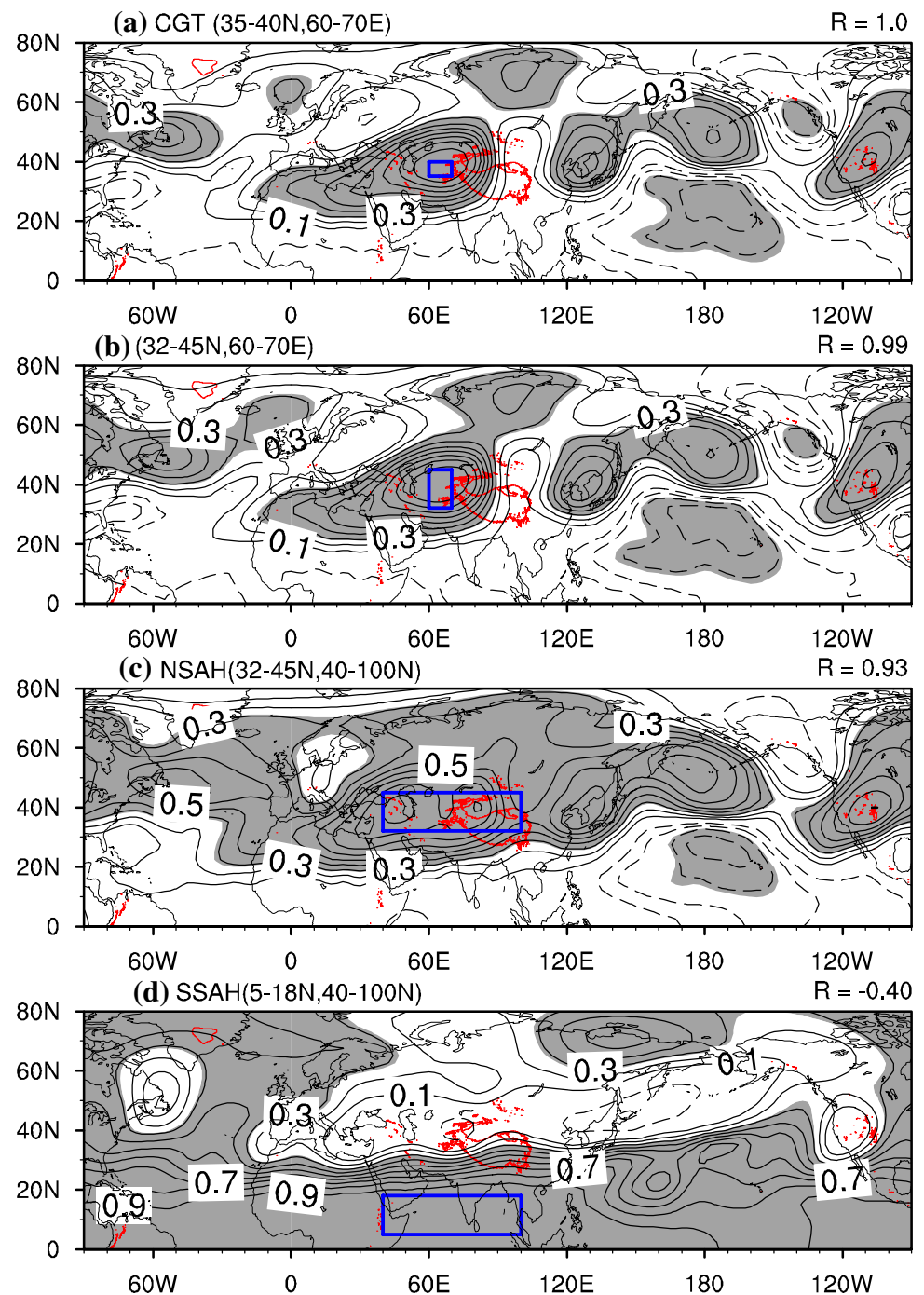
Since the distribution of HGT anomalies associated with N-SAH variation in Fig. 5c and d is similar to those of the circumglobal teleconnection (CGT; Ding and Wang 2005), the relationship of CGT with N-SAH was investigated. One-point correlation maps between several base points and summertime 150-hPa HGT are shown in Fig. 15. Based on the method in Ding and Wang (2005), one-point correlation map of 150-hPa HGT anomalies with reference to the HGT averaged over Uzbekistan and east Turkmenistan (35°–40°N, 60°–70°E) to describe the features of CGT in Fig. 15a. The characteristic is displayed by the one-point correlation map is that the HGT variations over northern Atlantic-western Europe, northeast China, North Pacific, and North America are almost in phase with the variations over west-central Asia, as revealed by the prominent positive correlations. By contrast, HGT variation over European Russia, upstream of the reference region, shows a weak negative correlation. The spatial pattern of the correlations in Fig. 15a is quite similar to the CGT pattern that is exhibited by the one-point correlation map in Fig. 1b of Ding and Wang (2005). In contrast, the variation over European Russia is weak and differs from that of Ding and Wang (2005), who obtained somewhat stronger negative center. This difference is likely due to that the present one-point correlation is based on 150-hPa HGT anomalies during 1980–2017, whereas Ding and Wang (2005)'s is based on 200-hPa HGT anomalies in 1948–2003. We expand the base point (35°–40°N, 60°–70°E) to (32°–45°N, 60°–70°E) and the CGT pattern are not affected, with pattern CC 0.99 (Fig. 15b). Furthermore, we also change the base point to (32°–45°N, 40°–100°E) and (5°–18°N, 40°–100°E), where utilized to define the N-SAH and S-SAH (Fig. 15c, d). It is

interesting to find that the pattern of the one-point correlation map associated with N-SAH is quite close to those of CGT, with pattern CC 0.93, indicating N-SAH variations is closely correlated with CGT (Fig. 15c). Whereas the one-point correlation map related to S-SAH is weakly connected to CGT, with pattern CC – 0.4 (Fig. 15d). Additionally, in order to further investigate the relationship of N-SAH and CGT, the interannual variability of 150-hPa averaged HGT over the reference area (35°–40°N, 60°–70°E) is employed to define CGT index. The CC between N-SAH and CGT index is 0.80, far exceeding 99% confidence level. Additionally, it is found that seven out of eleven strong CGT years (1984, 1990, 1994, 1998, 2006, 2008, 2013) and 8 out of 12 weak CGT years (1982, 1987, 1992, 1993, 2002, 2003, 2004, 2009) are accompanied by strong and weak N-SAH, respectively. Ding and Wang (2005) revealed that the Indian summer monsoon (ISM) can play an active role in the formation of CGT. A strengthened ISM tends to inducing an atmospheric heating source there via the increased rainfall over the Indian Peninsula (Fig. 9c). The atmospheric heating source over Indian Peninsula generates an upper-level abnormal high to its northwest over central Asia as a Gill-type wave response, which in turn generates an eastward downstream atmospheric wave train, forming the CGT (Fig. 15c). Then, the upper-level anomalous high over central Asia would exert impacts on the variations of the N-SAH. However, the CC of S-SAH and CGT is – 0.07, indicating that CGT is barely correlated with S-SAH variations.

5.4 The tropical SST related to ENSO event

Previous investigations have documented the close relationship between the El Niño–Southern Oscillation (ENSO) events and the SAH variations (Zhang et al. 2000; Xue et al. 2015, 2018). The ENSO exerts pronounced impact on the SAH via modulating the anomalous Walker circulation and charge effect over the tropical Indian

Fig. 15 One-point correlation map between base-point (blue boxes) **a** circumblobal teleconnection (CGT, 35°–40°N, 60°–70°E), **b** (32°–45°N, 60°–70°E), **c** N-SAH (32°–45°N, 40°–100°E), **d** S-SAH (5°–18°N, 40°–100°E) and summertime (JJA) 150-HGT for 1980–2017. The pattern correlation coefficients of CGT pattern with **a–d** are displayed at the top-right corners of each corresponding figure



Ocean (TIO) (Yang et al. 2007; Xie et al. 2009; Huang et al. 2011, Xue et al. 2015, 2018). SST warming (cooling) firstly occurs over TIO during boreal autumn following development of an El Niño (a La Niña) event, then the SST warming (cooling) attain its maximum during the following winter when El Niño (La Niña) achieves its highest phase (Klein et al. 1999; Lau and Nath 2000, 2003; Alexander et al. 2002; Xie et al. 2002). SST anomalies over TIO could sustain to the following summer after the

decaying of an El Niño (a La Niña) event (Xie et al. 2009; Du et al. 2009) and therewith exert far-reaching influence on the surrounding and remote climate (Annamalai et al. 2005; Yang et al. 2007; Xie et al. 2009). SST anomalies over the TIO during summer could generate impacts on the variability of the SAH through a Matsuno-Gill type (Matsuno 1966; Gill 1980) atmospheric response to the condensational heating related to precipitation anomalies (Yang et al. 2007; Li et al. 2008) and moisture adjustment

Table 4 CC between D(0)JF(1) Niño3 with various SAH indices

	N-SAH	S-SAH	E-SAH	<i>I</i> area	<i>I</i> inta	<i>I</i> intb	<i>I</i> intc
Niño3 (D(0)JF(1))	− 0.06	0.69*	0.44*	0.56*	0.43*	0.60*	0.36*
Niño3 (MAM(1))	− 0.23	0.66*	0.17	0.36*	0.18	0.40*	0.12
Niño3 (JJA(1))	− 0.40*	0.37*	− 0.27*	− 0.11	− 0.26	− 0.19	− 0.30*

The symbol of “*” denotes that the CC exceeds the 95% confidence level. Here the winter of 1992 (for instance) (D(0)JF(1)) refers to the winter 1991/1992

via modulating the tropospheric temperature (Huang et al. 2011; Qu and Huang 2012).

Accordingly, the correlation of ENSO with E-SAH, N-SAH, S-SAH are analyzed in this section. Table 4 shows the CC of Niño3 index during preceding winter (D(0)JF(1), here the winter of 1992 (for example) referring to the winter of 1991/1992), homochromous spring and summer (MAM(1), JJA(1)) with several SAH indices (N-SAH, S-SAH, E-SAH, *I*area, *I*inta, *I*intb, *I*intc). When the SAH is regarded as an entirety (for instance, E-SAH, *I*area, *I*inta, *I*intb, *I*intc), it is closely correlated with the preceding winter ENSO, which decays during the following spring and disappears in summer, consistent with those in the studying of Xue et al. (2015, 2018). The S-SAH is also closely correlated with Niño3 index during preceding winter always to following summer, with stronger and significant CC (0.69, 0.66, 0.37), indicating that the S-SAH variation is more prominently connected to ENSO than E-SAH. However, the association of the N-SAH with Niño3 index in preceding winter and spring is weak, with CC − 0.06 and − 0.23, respectively. In contemporaneous summer, the N-SAH is out of phase with Niño3 index with CC − 0.40, indicating the surface sea temperature (SST) over tropical eastern Pacific closely connected to the N-SAH variations in a way. Figure 16 displays the composite of SST anomalies in the strong and weak case of N-SAH and S-SAH. For S-SAH, prominent positive (negative) SST anomalies are observed over tropical eastern Pacific and tropical Indian ocean from contemporaneous spring to summer. This differs from those of E-SAH, which revealed the SST anomalies associated with ENSO have already disappeared during summer (Xue et al. 2015, 2018), indicating that the S-SAH variations are not only closely related to the SST anomalies over tropical Indian Ocean but also tropical eastern Pacific in contemporaneous summer. Nevertheless, for strong N-SAH, there are nearly no significant SST anomalies are observed over tropical Indian Ocean and Pacific except for warm anomalies over west northern Pacific in summer. For weak N-SAH, warm (cold) anomalies are remarkably observed over tropical eastern Pacific (northern Pacific) from spring to summer, whereas no significant SST anomalies existing over tropical Indian Ocean. Via checking the SST anomalies for weak N-SAH case in preceding autumn and winter, we find that an El Niño event begins in preceding winter, strengthens in

following summer, accompanied by no warming appearing over tropical Indian ocean. This differs from those associated E-SAH and S-SAH (figure not shown), which revealed that ENSO event begins in preceding spring, develops from preceding summer to autumn, peaks in preceding winter, then decays in following spring and summer, accompanied by prominent warming (cooling) existing over tropical Indian ocean from preceding autumn to following summer (Xue et al. 2018).

In the strong S-SAH phase (Fig. 7c), prominent tropospheric warming is observed over the tropics together with the TIO warming. The TT displays an obvious Rossby wave-like pattern with two maximum centers off the equator over the western TIO and a remarkable Kelvin wave pattern over the eastern TIO. The TT anomalies pattern is consistent to the Matsuno-Gill-like atmospheric response to tropical heating (Matsuno 1966; Gill 1980). Analogously, significant tropospheric cooling could be seen over the tropics accompanied by the TIO cooling in the weak S-SAH phase (Fig. 7f). The TT anomalies associated with E-SAH are similar with those of S-SAH except that it is a little bit weak. Furthermore, significant HGT anomalies could be observed over the tropics and southern Asia accompanied by remarkable SST anomalies over the TIO in S-SAH and E-SAH (Fig. 5a, b, e, f). This indicates that the TIO SST can exert impacts on TT and subsequently influence SAH variability in a way. By contrast, in the cases of strong and weak N-SAH, TT and 150-HGT anomalies over the tropics and southern Asia are very weak and insignificant (Figs. 5c, d, 7c, d). This further demonstrates that variation of the N-SAH is weakly associated with the TIO SST anomalies accompanied by the preceding winter ENSO events.

6 Summary and conclusion

Previous studies generally regarded the SAH as an entirety (referred to as E-SAH) ignoring its large meridional coverage, via defining intensity index as the area-averaged mean HGT over the region where the main body of SAH is located. However, in consideration of the large meridional coverage, variabilities of SAH may differ between the mid- to high-latitude and low-latitude region, and so may the impacted factors for the variations of northern and southern

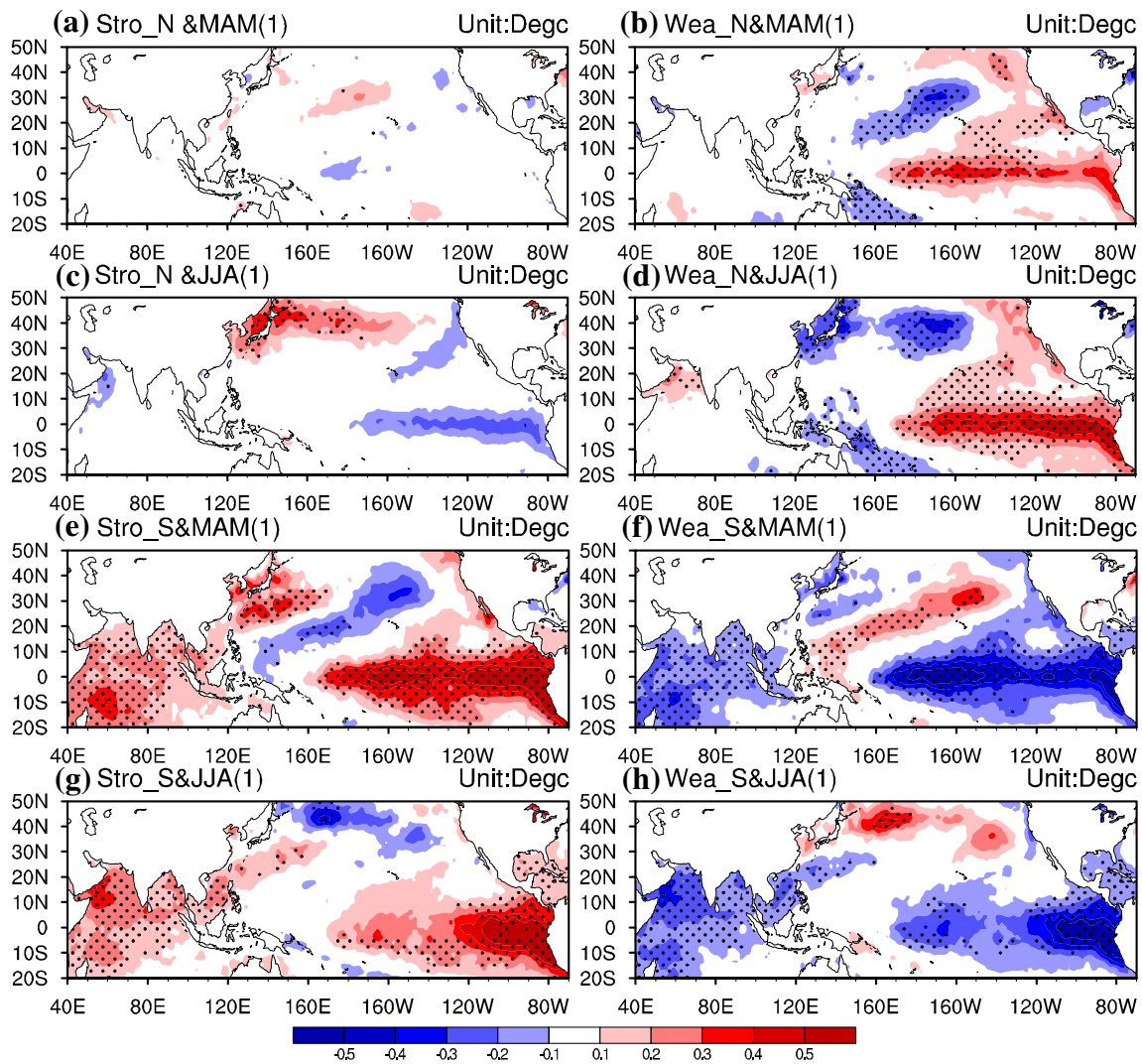


Fig. 16 Composite anomalies of SST (units: °C) for **a** strong N-SAH, **b** weak N-SAH during MAM(1) and **c** strong N-SAH, **d** weak N-SAH during JJA(1), respectively. **e–h** same as **a–d**, but for

the S-SAH cases. Stippled areas in **a–h** indicate regions where anomalies are significantly different from zero at the 95%

component of the SAH. Accordingly, the present study distinguishes the two components of the SAH variability in order to identify the respective features related to the northern and southern mode and the individual impacted factors of the two components variations. The northern and southern mode are ascertained by performing an EOF and REOF analysis of the 150-hPa summer HGT anomalies over Asia continent (0° – 50° N, 30° – 120° E) where the climatological SAH generally situated. Two indices have been defined to characterize the intensity of two modes of SAH, referred to as the N-SAHI and S-SAHI. The relationship of the two indices with those existing in previous studies are further investigated, and results indicate that the two indices are independent from each other, and can well describe the SAH variability.

Composite anomalies clearly demonstrate the respective characteristics unique to different types of E-SAH, N-SAH, and S-SAH. When the SAH is regarded as an entirety (E-SAH), it strengthens distinctly and expands toward meridional and zonal directions in strong E-SAH case. The HGT and TT anomalies associated with E-SAH are concurrently observed over the low-latitude and mid- to high-latitude region. In contrast, when the northern and southern mode of the SAH are defined (referred to as N-SAH, S-SAH) in the present study, the HGT and TT anomalies associated with the strong and weak N-SAH (S-SAH) are only observed over the mid- to high-latitude (low-latitude) region. The different features connected with N-SAH and S-SAH demonstrate that it is necessary and of scientific significance to distinguish the northern and southern mode of the SAH.

Possible impacted factors for the variations of the mid- to high-latitude and low-latitude component of the SAH are further analyzed. Particularly, the connections of rainfall anomalies, meridional circulation, the land surface temperature (LST), mid-latitude teleconnection CGT, and tropical SST anomalies with the SAH variability are investigated. For strong N-SAH case, the summer precipitation anomalies over Indian Peninsula are obviously more than normal. Significant ascending motion over southern TP (20°–35°N) and descending motion over northern TP (35°–50°N) forms a north-shifting meridional circulation over 20°–50°N. The decreased LST anomalies over Indian Peninsula caused by cloud-radiation feedback and the increased LST anomalies over northern TP by descending motion here form a southward LST gradient. The LST gradient from northern TP to Indian Peninsula will reduce the climatological surface temperature gradient from south to north, which widens wave movement and finally contributes to a strong N-SAH over north of 25°N. The positive precipitation anomalies over Indian Peninsula are conducive to a CGT pattern over mid-high latitude, which in turn strengthens the N-SAH. Similarly, for the weak N-SAH case, less than normal rainfall anomalies and descending (ascending) motion over Indian Peninsula (northern TP) lead to increased (decreased) LST anomalies here, which forms a south-to-north LST gradient and an opposite direction meridional circulation, finally contributes to weak N-SAH. For the S-SAH case, a remarkable meridional circulation can be still observed over southern TP (south of 35°N) though no significant rainfall anomalies existing here. Significant warm (cooling) LST anomalies associated with strong S-SAH (weak S-SAH) are observed over Indian Peninsula, which are affected by the warm (cooling) SST anomalies over Indian Ocean. A significant meridional circulation is formed over southern TP (south of 32°N) due to atmospheric response to the heating source generated by warm SST anomalies over Indian Ocean. Significant warm anomalies are observed to extend from low to upper troposphere over southern TP through Matsuno–Gill-like atmospheric response to tropical heating (Matsuno 1966; Gill 1980), which finally result in a strong and southward S-SAH. The process in weak S-SAH case is similar but out of phase with that in strong S-SAH. However, for the variation associated with E-SAH, it is a result of the combined action of rainfall anomalies over Indian Peninsula and SST anomalies over Indian Ocean. The ascending motion related with rainfall anomalies over Indian Peninsula enhances the upwelling branch induced by the tropical warming SST anomalies over Indian Ocean, which forms a strong ascending motion extending from Indian Ocean to southern TP. This finally contributes to a warm center and strong E-SAH over TP. These differences clearly reveal the necessity of distinguishing the two modes of the SAH to further understand the related impacted factors.

Acknowledgements We thank two anonymous reviewers for their constructive suggestions and comments, which helped to improve the paper. This study is supported jointly by the National Natural Science Foundation of China (Grant No. 41705069), the Science and Technology Project of Guizhou Province (Talents of Guizhou Science and Technology cooperation platform, [2017]5788), and the Scientific Research Project of Introduced Talents of Guizhou University (No. 2016(34)). The authors declare that they have no conflict of interest.

References

- Alexander MA, Blade I, Newman M, Lanzante JR, Lau NC, Schott JD (2002) The atmospheric bridge: the influence of ENSO teleconnections on air-sea interaction over the global oceans. *J Clim* 15:2205–2231
- Annamalai H, Liu P, Xie SP (2005) Southwest Indian Ocean SST variability: its local effect and remote influence on Asian monsoons. *J Clim* 18:4150–4167
- Cai XC, Li Y, Zhang XK, Bao YY (2017) Characteristics of South Asia high in summer in 2010 and Its relationship with rainbands in China. *J Geosci Environ Protect* 5:210–222
- Chen W, Zhu DQ, Liu HZ, Sun SF (2009) Land-air interaction over arid/semi-arid areas in China and its impact on the east Asian summer monsoon part I: calibration of the land surface model (BATS) using multicriteria methods. *Adv Atmos Sci* 26:1088–1098
- Dee DP et al (2011) The ERA-interim reanalysis: configuration and performance of the data assimilation system. *Q J R Meteor Soc* 137:553–597
- Deth A, O'Neill A, Slingo JM, Smit HGJ (1999) A mechanism for moistening the lower stratosphere involving the Asian summer monsoon. *Q J R Meteor* 125:1079–1106
- Ding QH, Wang B (2005) Circumglobal teleconnection in the Northern Hemisphere summer. *J Clim* 18:3483–3505
- Du Y, Xie SP, Huang G, Hu KM (2009) Role of air-sea interaction in the long persistence of El Niño-induced North Indian Ocean warming. *J Clim* 22:2023–2038
- Fitzpatrick PJ, Knaff JA, Landsea CW, Finley SV (1995) A systematic bias in the Aviation model's forecast of the Atlantic tropical upper tropospheric trough: implications for tropical cyclone forecasting. *Weather Forecast* 10:433–446
- Flohn H (1957) Large-scale aspects of the summer monsoon in South and East Asia. *J Meteor Soc Jpn* 75:180–186
- Flohn H (1960) Recent investigations on the mechanism of the "Summer Monsoon" of Southern and Eastern Asia. *Proc Symp Monsoon of the World*. Hind Union Press, New Delhi, pp 75–88
- Ge J, You QL, Zhang YQ (2018) Interannual variation of the northward movement of the South Asian High towards the Tibetan Plateau and its relation to the Asian summer monsoon onset. *Atmos Res* 213:381–388
- Gill AE (1980) Some simple solutions for heat-induced tropical circulation. *Q J R Meteor Soc* 106:447–462
- Hannachi A, Jolliffe IT, Stephenson DB (2007) Empirical orthogonal functions and related techniques in atmospheric science: a review. *Int J Climatol* 27:1119–1152
- Harris IC, PD Jones (2017) CRU TS4.01: Climatic Research Unit (CRU) Time-Series (TS) version 4.01 of high-resolution gridded data of month-by-month variation in climate (Jan. 1901–Dec. 2016). Centre for Environmental Data Analysis, 04 Dec 2017. <https://doi.org/10.5285/58a8802721c94c66ae45c3baa4d814d0>
- Horel JD (1981) A rotated principal component analysis of the interannual variability of the Northern Hemisphere 500 mb height field. *Mon Weather Rev* 109:2080–2092

- Huang G, Qu X, Hu KM (2011) The impact of the tropical Indian Ocean on South Asian High in boreal summer. *Adv Atmos Sci* 28:421–432
- Kaiser HF (1958) The Varimax criterion for analytic rotations in factor analysis. *Psychometrika* 23:187–220
- Kalnay E, Kanamitsu M, Kistler R, Collins W, Deaven D, Gandin L, Iredell M, Sana S, White G, Woollen J, Zhu Y, Chelliah M, Ebisuzaki W, Higgins W, Janowiak J, Mo KC, Ropelewski C, Wang J, Leetmaa A, Reynolds R, Jenne R, Joseph D (1996) The NCEP/NCAR 40-year reanalysis project. *Bull Am Meteorol Soc* 77:437–471
- Kelley WE, Mock DR (1982) A diagnostic study of upper tropospheric cold lows over the western North Pacific. *Mon Weather Rev* 110:471–480
- Klein SA, Soden BJ, Lau NC (1999) Remote sea surface temperature variations during ENSO: evidence for a tropical atmospheric bridge. *J Clim* 12:917–932
- Krishnamurti TN (1971) Tropical east–west circulations during the northern summer. *J Atmos Sci* 28:4366–4377
- Krishnamurti TN, Daggupati SM, Fein J, Kanamitsu M, Lee JD (1973) Tibetan High and upper tropospheric tropical circulation during northern summer. *Bull Am Meteor Soc* 54:1234–1249
- Lau NC, Nath MJ (2000) Impact of ENSO on the variability of the Asian–Australian monsoons as simulated in GCM experiments. *J Clim* 13:4287–4309
- Lau NC, Nath MJ (2003) Atmosphere–Ocean variations in the Indo-Pacific sector during ENSO episodes. *J Clim* 16:3–20
- Li Q, Jiang J, Wu DL, Read WG, Livesey NJ et al (2005) Convective outflow of South Asian pollution: A global CTM simulation compared with EOS MLS observations. *J Geophys Lett* 32:L14826. <https://doi.org/10.1029/2005gl022762>
- Li SL, Lu J, Huang G, Hu KM (2008) Tropical Indian Ocean basin warming and East Asian summer monsoon: a multiple AGCM study. *J Clim* 21:6080–6088
- Li H, He S, Fan K, Wang HJ (2018) Relationship between the onset date of the Meiyu and the South Asian anticyclone in April and the related mechanisms. *Clim Dyn*. <https://doi.org/10.1007/s00382-018-4131-5>
- Liu YM, Wu GX, Ren RC (2004) Relationship between the subtropical anticyclone and diabatic heating. *J Clim* 17:682–698
- Luo SW, Chen ZA, Wang QQ (1982) The climatic and synoptical study about the relation between the Qinhai–Xizang high pressure on the 100-mb surface and the flood and drought in east China in summer (in Chinese). *Plateau Meteorol* 1:1–10
- Mason RB, Anderson CE (1963) The development and decay of the 100-MB. Summertime anticyclone over Southern Asia. *Mon Weather Rev* 91:3–12
- Matsuno T (1966) Quasi-geostrophic motions in the equatorial area. *J Meteorol Soc Jpn* 44:25–43
- Ning L, Liu J, Wang B (2017) How does the South Asian High influence extreme precipitation over eastern China? *J Geophys Res* 122:4281–4298
- Park M, Randel WJ, Kinnison DE, Garcia RR, Choi W (2004) Seasonal variation of methane, water vapor, and nitrogen oxides near the tropopause: satellite observations and model simulations. *J Geophys Res* 109:D03302. <https://doi.org/10.1029/2003JD003706>
- Park M, Randel WJ, Emmons LK, Bernath PF, Walker KA, Boone CD (2008) Chemical isolation in the Asian monsoon anticyclone observed in atmospheric chemistry experiment (ACE-FTS) data. *Atmos Chem Phys* 8:757–764
- Qian YF, Zhang Q, Yao YH, Zhang XH (2002) Seasonal variation and heat preference of the South Asia High. *Adv Atmos Sci* 19(5):821–836
- Qu X, Huang G (2012) An enhanced influence of tropical Indian Ocean on the South Asia high after the late 1970s. *J Clim* 25:6930–6941
- Randel WJ, Park M (2006) Deep convective influence on the Asian summer monsoon anticyclone and associated tracer variability observed with Atmospheric Infrared Sounder (AIRS). *J Geophys Res* 111:D12314. <https://doi.org/10.1029/2005JD006490>
- Rayner NA, Brohan P, Parker DE, Folland CK, Kennedy JJ, Vanicek M, Ansell TJ, Tett SFB (2006) Improved analyses of changes and uncertainties in sea surface temperature measured in situ since the mid-nineteenth century: the HadSST2 dataset. *J Clim* 19:446–469
- Ren XJ, Yang DJ, Yang XQ (2015) Characteristics and mechanisms of the subseasonal eastward extension of the South Asian High. *J Clim* 28:6799–6822
- Richman MB (1986) Rotation of principal components. *J Climatol* 6:293–335
- Sadler JC (1976) A role of the tropical upper tropospheric trough in early season typhoon development. *Mon Weather Rev* 104:1266–1278
- Shi J, Qian WH (2016) Connection between anomalous zonal activities of the South Asian High and Eurasian summer climate anomalies. *J Clim* 29:8249–8267
- Tao SY, Chen LX (1987) A review of recent research on the East Asian summer monsoon in China. In: Krishnamurti TN (ed) *Change CP. Monsoon meteorology* Oxford University Press, Oxford, pp 60–92
- Tao SY, Zhu FK (1964) The 100-mb glow patterns in southern Asia in summer and its relation to the advance and retreat of the West-Pacific subtropical anticyclone over the Far East. *Acta Meteorol Sin* 34:385–396 (in Chinese)
- Wei W, Zhang RH, Wen M (2012) Meridional variation of South Asian High and its relationship with the summer precipitation over China. *J Appl Meteor Sin* 23(6):650–659 (in Chinese)
- Wei W, Zhang RH, Wen M, Kim BJ, Nam JC (2014) Interannual variation of the South Asian high and its relation with Indian and East Asian Summer monsoon rainfall. *J Clim* 28:2623–2634
- Wei W, Zhang RH, Wen M, Kim BJ, Nam JC (2015) Interannual variation of the South Asian high and its relation with Indian and East Asian Summer monsoon rainfall. *J Clim* 28:2623–2634
- Wei W, Zhang RH, Wen M, Yang S (2017) Relationship between the Asian westerly jet stream and summer rainfall over central Asia and north China: roles of the Indian monsoon and the south Asian high. *J Clim* 30:537–551
- Wu L, Wang C (2015) Has the western Pacific subtropical high extended westward since the late 1970s? *J Clim* 28:5406–5413
- Wu ZW, Zhang P, Chen H, Li Y (2016) Can the Tibetan Plateau snow cover influence the interannual variations of Eurasian heat wave frequency? *Clim Dyn* 46:3405–3417
- Xie SP, Annamalai H, Schott FA, McCreary JP (2002) Structure and mechanism of south Indian Ocean climate variability. *J Clim* 15:864–878
- Xie SP, Hu KM, Hafner J, Tokinaga H, Du Y, Huang G, Sampe T (2009) Indian Ocean capacity effect on Indo-western Pacific climate during the summer following El Niño. *J Clim* 22:730–747
- Xue X, Chen W, Zhou DW, Nath D (2014) Whether the decadal shift of South Asia High intensity around the late 1970s exists or not. *Theor Appl Climatol* 120(3):673–683
- Xue X, Chen W, Chen SF, Zhou DW (2015) Modulation of the connection between boreal winter ENSO and the South Asian High in the following summer by the stratospheric Quasi–Biennial Oscillation. *J Geophys Res Atmos* 120:7393–7411. <https://doi.org/10.1002/2015JD023260>
- Xue X, Chen W, Chen SF (2017) The climatology and interannual variability of the South Asia high and its relationship with ENSO in CMIP5 models. *Clim Dyn* 48:3507–3528
- Xue X, Chen W, Chen SF, Feng J (2018) Modulation of the connection between boreal winter ENSO and the following summer South Asian High by the PDO. *Clim Dyn* 50:1393–1411
- Yang JL, Liu QY, Xie SP, Liu ZY, Wu LX (2007) Impact of the basin-wide mode of the Indian Ocean SST basin mode on the Asian

- summer monsoon. *Geophys Res Lett* 24:L02708. <https://doi.org/10.1029/2006GL028571>
- Zhang Q, Qian YF, Zhang XH (2000) The interannual and interdecadal change of South Asia high. *Chin J Atmos Sci* 24(1):67–78 (in Chinese)
- Zhang Q, Wu GX, Qian YF (2002) The Bimodality of the 100 hPa South Asia High and its Relationship to the Climate Anomaly over East Asia in Summer. *J Meteor Soc Jpn* 80(4):733–744
- Zhang PQ, Yang S, Kousky VE (2005) South Asian high and Asian–Pacific–American climate teleconnection. *Adv Atmos Sci* 22:915–923
- Zhao P, Zhang X, Li Y, Chen J (2009) Remotely modulated tropical North Pacific ocean–atmosphere interactions by the South Asian high. *Atmos Res* 94:45–60
- Zhu FK, Lu LH, Chen XJ (1980) South Asian high. Beijing Science Press, Beijing, pp 1–94 (in Chinese)

Publisher's Note Springer Nature remains neutral with regard to jurisdictional claims in published maps and institutional affiliations.